Polarization Effects of Mechanical Impacts on Dispersion Compensating Modules

by

Derek Dumas

A thesis
presented to the University of Waterloo
in fulfillment of the
thesis requirement for the degree of
Master of Science
in
Physics

Waterloo, Ontario, Canada, 2009

I hereby declare that I am the sole author of this thesis. This is a true copy of the thesis, including any required final revisions, as accepted by my examiners.

I understand that my thesis may be made electronically available to the public.

Abstract

Novel methods and apparatus used to measure high-speed state of polarization changes are developed. Knowledge of the effects of mechanical impacts on the state of polarization will benefit the reliability of optical communication systems. The impact creates a high-speed but continuous motion of the state of polarization over the Poincaré sphere. The maximum speed at which the state of polarization changes due to an impact is shown to be higher than what has been reported previously.

The investigation into the state of polarization changes led to the discovery of the repeatability and elasticity of state of polarization changes due to mechanical impacts. The repeatability and elasticity allow novel measurements of important polarization effects in optical fibres such as high-speed polarization mode dispersion and rotation vector measurements.

Acknowledgements

I would like to thank my supervisor, Dr. David Yevick, for the guidance and support during my work. I would also like to thank Mr. Michael Reimer, for all his help and advice. Support for this thesis was also provided by Ontario Graduate Scholarship (OGS), Nortel, and the University of Waterloo.

Dedication

To Paula

Contents

List of Tables

List of Figures

Table of Symbols

Symbol	Definition	Page
v	Phase velocity of light	2
c	Speed of light constant	2
n	Index of refraction	2
$S0, S1, S2, S3$	Stokes parameters	2
$s1, s2, s3$	normalized Stokes parameters	3
$\Gamma(t)$	rate of photon arrival at time t	8
P	Optical power	8
h	Plank constant	8
f	Frequency of light	8
$v_{\text{sop}}(t)$	Angular speed of SOP at time t	25
θ	Angular separation between states of polarization	27
$\hat{s}(t)$	Measured state of polarization at time t	27
$\hat{p}(t)$	True state of polarization at time t	27
$\mathbf{R}$	Rotation matrix	27
$\mathbf{B(t)}$	Matrix of SOP at time t	38
$\mathbf{A}$	Matrix of SOP at time $t = 0$	38
$.^T$	Matrix or vector transpose	38
$\times$	Cross product operator	40
$\vec{r}(t)$	Rotation vector at time t	40
$\hat{a}(t)$	Normalized rotation vector at time t	40
$\mathbf{I}$	Identity matrix	40
$DFT(\cdot)$	Discrete Fourier transform	41
x_i	ith component of a vector	41
y_i	Fourier transform of x_i	41

Symbol	Definition	Page
Y	Spectrum of frequencies of time dependent vector	41
σ	Standard deviation of noisy data	45
Y_{p}	Power in spectrum of rotation vector frequencies	42
$\vec{V}$	Derivative of the rotation vector	45
E_{sq}	Sum of squared error of $\vec{V}$	46
$\vec{r}\,'$	Derivative of rotation vector with respect to time	47

Chapter 1

Introduction

Optical communications are a key element of the world-wide information transfer structure. Optical fibre networks connecting cities together currently allow high quality and rapid data exchange between almost any pair of cities in the world. With the ever-increasing demand for data transmission, higher speeds and more complex encoding methods are required to convey the maximum possible amount of data through pre-installed fibres. However, some rapid changes in the polarization dependent behaviour of the pulse response cannot be easily compensated. Uncompensated fluctuations can lead to infrequent system outages in currently installed fibres that inhibit the adoption of high data rate systems.

In this thesis, we investigate polarization mode dispersion (PMD), which can severely limit the achievable rate of data transmission. In particular, if the PMD varies sufficiently slowly, it can be compensated optically or electronically. Thus characterizing and modelling the speed of the change in PMD is an important aspect of compensation system design. Since the time scale of PMD change is related to the correlation time of polarization changes, polarization measurements reveal the general behaviour of the fibre link.

In this chapter, Section 1.1 discusses basic electromagnetic theory of relevance to optical communications. Next, Section 1.2 summarizes optical fibre properties. The structure of optical communications systems is examined in Section 1.3. Section 1.4 considers optical data transmission and important optical system impairments. In the final section, we describe our experimental work and its relationship to previous research.

1.1 Properties of Light

1.1.1 Wave Properties of Light

Since light travels as an electromagnetic wave, [6] fibres can be designed to support a single mode (of two polarizations) that exhibits minimal dispersion, enabling high-speed transmission in long distance communication networks. Light waves in a homogeneous non-birefringent medium consists of transverse electric and magnetic field components which oscillate in time and space.[10] The distance the light travels during one period of temporal oscillation is its wavelength. The index of refraction (n) of a material determines the phase velocity of the light (Eq. 1.1)

$$v = c/n \tag{1.1}$$

where c is the speed of light in vacuum. For optical fibres a typical value of n is around 1.5, and the velocity of light in a fibre is therefore $\frac{2}{3}c$.

1.1.2 Polarization

Another property of light that is important to optical communications is polarization. Since modal fields in a fibre exist in different polarizations, the evolution of the field direction (field polarization) with time at a given position along the direction of travel has a different effect on the delay time of each modal field polarization. The electric field vector in a locally homogeneous medium can be projected into any two orthogonal directions perpendicular to the direction of travel. In this thesis, we specify the direction of travel as the z-axis and project two electric field vector components along the x and y axes.[9] The reference frame for these axes is generally taken to be the laboratory frame. For linearly polarized light, these x and y polarizations oscillate either in phase or 180° out of phase. Circular polarization, for which the electric field vector oscillates around a circular path, instead occurs when the two orthogonal components are equal in amplitude but oscillate out of phase by an odd multiple of a quarter of the light wavelength. A field that is neither linearly nor circularly polarized is termed elliptically polarized.

1.1.3 Poincaré Sphere

The state of polarization of light in an optical fibre can be specified in terms of the Stokes parameters $S0$, $S1$, $S2$, $S3$, which are respectively the total intensity

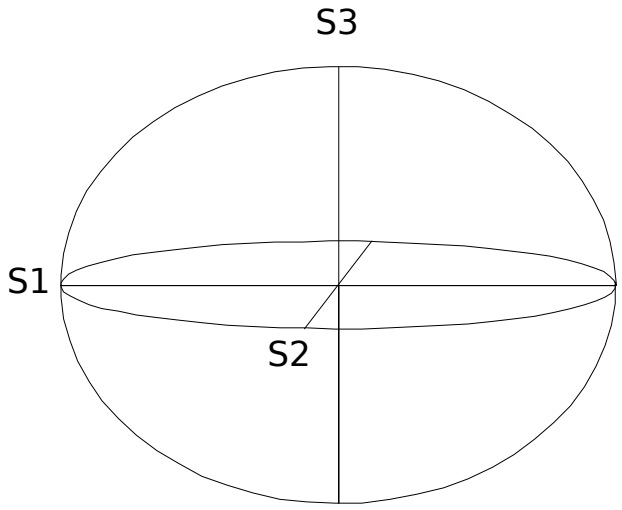

Figure 1.1: Poincaré sphere

of electric field, the field intensity in the horizontal linear polarization minus the intensity of the field in the vertical linear polarization, the intensity of the field in the 45° linear polarization state minus the intensity of the field in the −45° state, and the intensity of the field in the left-hand circular polarization state minus the intensity of the field in the right-hand state. The Stokes parameters can be simplified for fully polarized light for which the total power can be normalized to one and the Stokes parameters $s1, s2, s3$ defined by (Eq. 1.2).

$$sj = \frac{Sj}{\sqrt{S1^2 + S2^2 + S3^2}}, j = 1, 2, 3 \tag{1.2}$$

can then be employed. The resulting sphere, shown in Fig. 1.1, was introduced by Poincaré in 1892 [24]. Each position on the sphere corresponds to a unique polarization state. The states located along the equator correspond to linearly polarized light while the two states at the north and south poles represent the two states of circular polarization. The remainder of the sphere maps to the elliptically polarized states. Hence any point on the sphere yields a unique state of polarization with normalized Stokes parameters $\{x, y, z\} \rightarrow \{s1, s2, s3\}$.

1.2 Optical Fibres

1.2.1 Physical Properties

Fibres in optical fibre networks are formed from glass with doping concentration variations that induce a spatially varying refractive index profile.[4] A single mode

communications fibre possesses a high-index core with a diameter of the order of 8μm that is typically doped with germanium, surrounded by a lower index cladding region with a much larger diameter, for example 125μm, generally composed of pure silica glass. The higher refractive index of the core enables the total internal refraction of rays with a large incidence angle that are directed primarily in the z, propagation, direction. To produce high quality modern optical fibres, the index of refraction profile of the core and cladding are carefully controlled. First preforms with carefully graded dopant concentrations and therefore refractive index variations are formed. These are then drawn into fibres with lengths of up to several hundred kilometres.

1.2.2 Power Attenuation

Light is attenuated as it travels through optical fibres as a result of numerous physical effects including Rayleigh scattering, absorption due to metallic impurities and water in the fibre, and intrinsic absorption by the silica molecule itself. Rayleigh scattering, the scattering of light due to small inhomogeneities as it propagates through a medium, is wavelength dependent since shorter wavelengths scatter more than longer wavelengths. Impurities in the fibre such as metal ions and water in the glass produce a power loss through absorption and scattering. In fact, metal ions at levels of one part per billion could increase the attenuation by 1 dB/km, and water at levels of one part per million could increase the attenuation by 4 dB/km. However, with modern fibre production techniques, these impurities can be reduced to a negligible level. At wavelengths longer than 1650nm the intrinsic infrared absorption of light due to vibrational resonances in silica becomes appreciable. If all impurities are eliminated, light at 1550 nm still experiences a theoretical attenuation of 0.16 dB/km. Commercially available fibres accordingly display minimum attenuations as low as 0.19 dB/km.[23]

1.2.3 Power Amplification

Attenuation in optical fibre networks can be compensated along the fibre span by optical amplifiers, such as the erbium doped fibre amplifier (EDFA), or by repeaters which decode and retransmit data. An EDFA is a short length of fibre which amplifies the signal light by stimulated emission. The energy for amplification is obtained from a "pump laser" that excites the erbium ions in this section of fibre. An EDFA increases light amplitude without affecting the pulse shape. A repeater

is a transceiver which reads the data and retransmits the information. A repeater must be designed for the bit rate and type of signal being transmitted, and replaced or upgraded when the signal is upgraded. The EDFA is independent of the signal bit rate and type, which makes upgrades in EDFA links simple and inexpensive.

1.2.4 Chromatic Dispersion

Signal degradation in optical fibre networks also results from chromatic dispersion. Chromatic dispersion refers to the pulse broadening induced by the differing phase velocities of different wavelengths. Pulse broadening causes intersymbol interference, which implies that the signal from one bit overlaps with light from adjacent bits. When intersymbol interference is present, the power in a given bit is affected by the bit pattern. Two principle forms of chromatic dispersion exist in single mode fibres: waveguide dispersion, which results from the geometry of the fibre waveguide, and material dispersion, which is induced by the intrinsic wavelength dependence of the refractive index of glass. The net dispersion of a fibre can be either positive or negative. When the dispersion is positive longer wavelengths travel slower than shorter wavelengths while the opposite is true for negative dispersion. The amount of material and waveguide dispersion, as well as the total dispersion, is wavelength dependent[23] and can be controlled by changes to the fabrication of the fibre induced by the dopant levels and core diameter. Fibres can therefore be fabricated that display zero dispersion at specified wavelengths. Fibres can also be designed to have a high negative dispersion. These are called dispersion compensating fibres. Dispersion compensating fibres are often packaged as dispersion compensating modules that can be employed to reverse the chromatic dispersion of a standard fibre.

1.2.5 Dispersion Compensating Modules

Millions of kilometres of optical fibre are currently deployed that are dispersion shifted to insure zero dispersion at a wavelength of 1310nm. Since light at 1550nm experiences minimum attenuation in a fibre and falls within the operational band of the current generation of EDFAs, this wavelength is preferred for optical fibre networks. Currently installed legacy dispersion shifted fibre however possesses typical dispersion around $17 ps/km \cdot nm$ at 1550nm. While this value is associated with large pulse distortion, replacing the fibre with low dispersion fibre would be prohibitively expensive. Consequently, dispersion compensating modules (DCMs)

are used at the ends of the links to reverse the dispersion. These modules contain a tightly wound spool of dispersion compensating fibre (DCF) wrapped around a metal core and sealed within a metal box. The DCF in turn is an optical fibre designed to exhibit a large negative dispersion on the order of $-100ps/km \cdot nm$ at 1550nm. The length of DCF in a DCM is calibrated to reduce the total dispersion of the link fibre and the DCM to a near-zero value. For fibres with these levels of dispersion, approximately 17km of DCF is typically required for every 100km of standard fibre.

1.2.6 PMD and PDL

Polarization mode dispersion (PMD) refers to the pulse broadening caused by the net fibre birefringence. Birefringence is generated when light polarized along each of the two principal polarization axes experiences a different average index of refraction and group velocity. In this case, one of these two polarizations will experience a greater group delay than the other polarization. The birefringence changes along the length of the fibre and as a function of time resulting in a randomly varying distortion. This PMD-induced pulse distortion limits the speed of current communications systems, and must be actively compensated due to its time varying nature. Polarization dependent loss (PDL) occurs when the attenuation of the light is dependent on its polarization. PDL both rotates the state of polarization and affects the relative power in the two polarizations.

1.2.7 SOP Rotation

When light is launched into a single mode fibre, the light polarization has different projections along two orthogonally polarized (in the absence of polarization dependent loss) "principal axes" of the birefringence, which we take to be the x and y axes. In a circular fibre and in the absence of stresses, these polarizations would be degenerate. In practise, single mode fibres possess different effective indices of refraction due to internal or external mechanical stresses, a non-circular core, bending or the presence of electrical and magnetic fields.[20] This birefringence leads to orthogonal polarizations having different group velocities as well as differing relative phases at the output. Only if these components are identical, however, will the state of polarization at the output be the same as the input state. As well, in most fibres the external stresses change with time as a result of temperature changes, vibrational noise, and other physical effects.

1.3 Optical Communications

1.3.1 Optical Communications Networks

Communications networks consist of hubs and connections between hubs. In optical communications networks, the hubs are generally located in or near cities, and each hub is connected to several other hubs in nearby cities.[21] Some coastal hubs are connected to each other via undersea links. [8] Each hub receives incoming data and transmits the data either along a link to another hub or to a local address.

1.3.2 Optical Communications Links

Communication links employ optical fibres, repeaters, compensators, transmitters, and receivers. In modern links EDFAs replace electronic repeaters, and undersea links also contain power transmitting wires along the fibre cables. Signal degradation during transmission results from attenuation, chromatic dispersion, PDL and PMD. In older links, the resulting distortion and attenuation is compensated by repeaters. These contain a receiver and transmitter pair that read the digital signal and subsequently retransmit the data after eliminating most or all of the accumulated distortion from the optical fibre. [6] In newer links EDFAs instead compensate the attenuation along the link, while DCMs counteract chromatic dispersion. The PMD and PDL however vary with time due to environmental factors such as temperature and vibration and thus must be actively monitored to facilitate compensation.

1.3.3 Optical Communication Hubs

Optical hubs, which are located at the ends of optical fibre links, contain the hardware, in particular transmitters and receivers that route the incoming signal to the next hub or network. Such hubs often include compensators such as DCMs that counteract the distortion of the optical signal by the transmission medium. However, such units can be accessed by personnel and can therefore be disturbed by work on or in the vicinity of the device.

1.4 Optical Data Encoding

1.4.1 Transmission Errors

An error in the transmission of a (non-corrected) signal in a digital communications system occurs if the receiver circuitry interprets a 1 bit as a 0 bit or vice-versa. In general, if the number of detected photons is smaller than a certain decision threshold during the bit timeslot, the bit is interpreted as a 0 bit; otherwise it is considered a 1 bit. Detection theory requires a semi-classical approach where the light is viewed as a stream of photons. The rate of photons Γ at a time t is related to the optical power P at time t by (Eq. 1.3).

$$\Gamma(t) = \frac{P(t)}{hf}\text{photons/s} \tag{1.3}$$

Photon arrival statistics for a coherent source follow a Poisson process in which the photon intensity Γ corresponds to a certain average number of photons during a period of time T. This probability distribution is shown in Fig. 1.2 for different values of Γ within one bit period. Thermal noise generates an additional current in the photodiode circuit which in turn can result in a fictitious detection of photons. The number of these additional photons is a Gaussian random variable.[8] Fig. 1.3 illustrates the potential impact of chromatic dispersion on a sequence of bits transmitted through a fibre [19]. Other sources of pulse broadening produce similar effects. The Poisson and thermal noise processes impart a random component to the number of detected photons, while pulse broadening results in an overlap of adjacent pulses. Such effects yield errors in the detection of the transmitted bits.

1.4.2 Error Handling

Errors in digital communication transmissions can be corrected by incorporating redundant information into the transmitted data. The information to be transmitted is encoded onto a larger data set such that an error in a small number of bits does not induce an error in the transmitted data. This error-correction coding enables the error-free transmission of information if the number of errors in a frame is less than a code-dependent threshold, above which data will be lost. To correct a high density of errors in this manner however requires a large number of extra symbols.[5][18] The amount of redundancy is governed by the system requirements so that a balance between error correction and information-carrying capacity must be established through detailed system design.

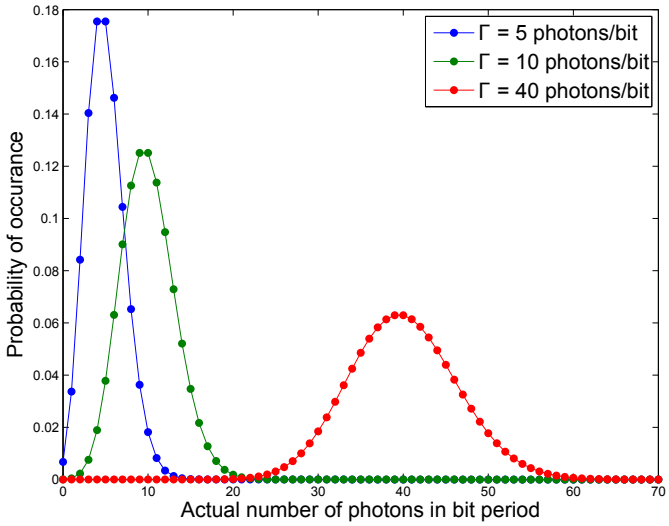

Figure 1.2: The Poisson distribution of the probabilities of recieving different numbers of photons during a bit period for intensities averaging 5, 10, and 40 photons per bit

1.4.3 On-Off Keying

The most common encoding method for optical communications is on-off keying (OOK). With OOK, data is encoded by modulating the laser according to the bit sequence and the coding scheme. For example, a non-return to zero (NRZ) code turns the laser on for a 1 bit and off for a 0 bit. In a return to zero (RZ) code, the laser instead is turned on for part of a bit period for a one and off for the rest of the bit and stays off for a zero.[16]

Another procedure for data encoding is amplitude shift keying, in which each symbol carries more than one bit of information, by accordingly modulating the light among levels of different amplitude. Amplitude shift keying is rarely employed since it requires a far higher signal to noise ratio than OOK for equivalent error probabilities. [8]

1.4.4 Advanced Encoding Methods

Recently proposed advanced encoding methods for optical communications encode data through polarization modulation. One method encodes two OOK bit patterns simultaneously on orthogonal polarizations. Ideally this yields two independent data signals, but state of polarization (SOP) rotations can mix the two signals. A similar but much more advanced method employs the two orthogonal polariza-

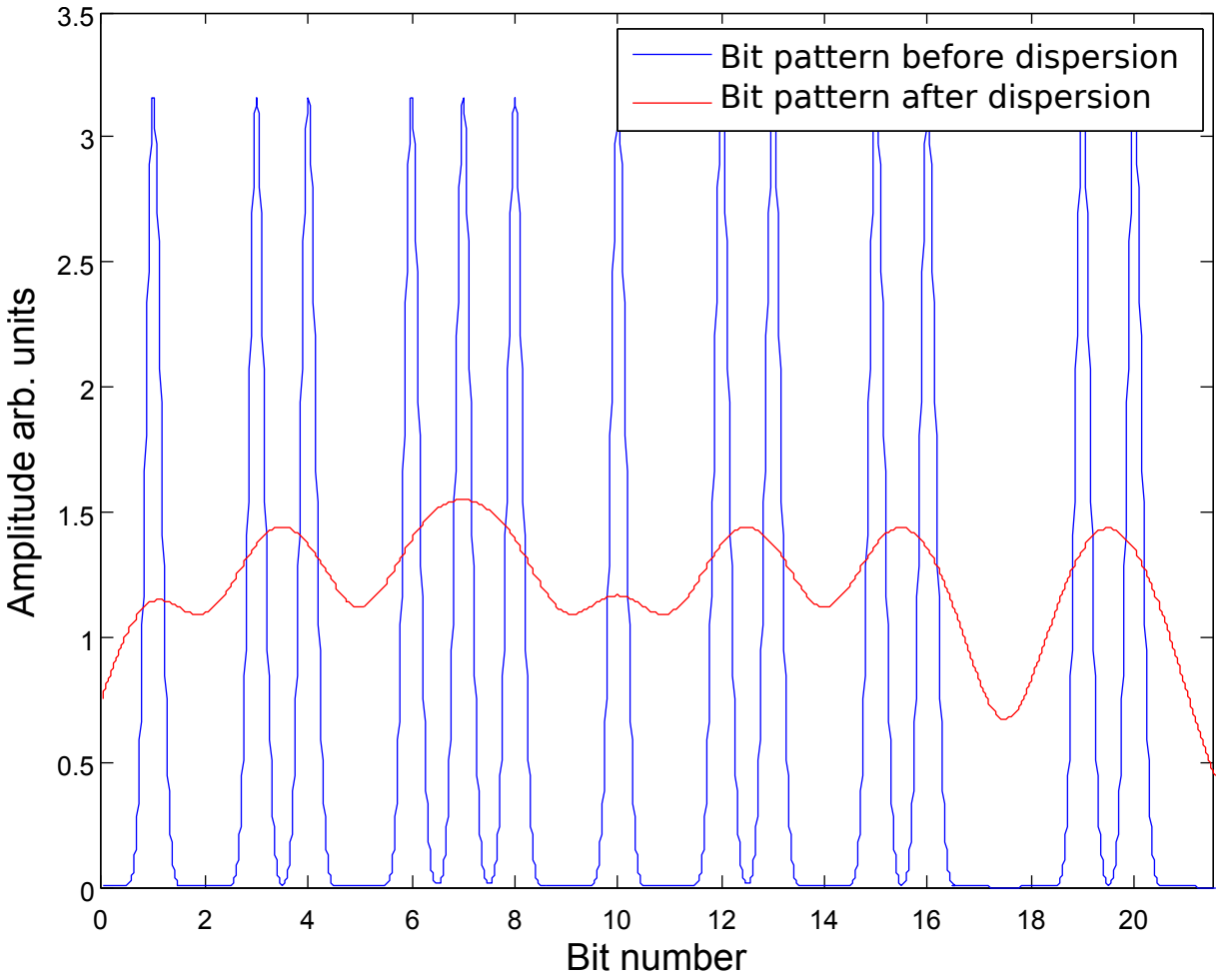

Figure 1.3: The optical amplitude of a series of bits in the absence (blue) and presence (red) of chromatic dispersion. Note the intersymbol interference resulting from pulse spreading into a neighbouring bit frames

tions by transmitting quadrature phase shift keying (QPSK) data along each axis. Another method is differential polarization shift keying (DPolSK), in which a polarization shift of π radians would signal a 1 bit while the absence of a shift signals a 0 bit. [13] In these modulation schemes the data depends on the SOP of the light, so that rotations in the SOP generated by link components limit the receiver's ability to decode the message. [26]

Rapid polarization changes do not affect the bit error rate of the system to decode the bits properly for polarization independent encoding methods. Even polarization dependent encoding methods are unaffected by polarization changes if these are far slower the symbol rate and are properly compensated. However, uncompensated or improperly compensated PMD degrades performance as a result of the mixing of light in different polarizations as well as between different time slots. Since PMD can vary with time it requires active compensation. Outages occur if the PMD of a system changes too rapidly for any active compensators present in the system to restore the signal. These PMD changes are generally caused by the same processes that affect the polarization state of the output electric field.

1.5 Rapid Polarization Measurements

Interest in rapid polarization measurements as applied to optical communications was principally the result of the work of Krummrich and Kotten who showed [17] that high-speed oscillations in the SOP result from modest mechanical impacts on DCMs. In their experiments mechanical vibrations were induced by dropping the DCM onto a hard surface, and hitting with metal tools. Their investigation was limited to examining the effect of uncontrolled impact events. Only the state of polarization was measured and the repeatability of similar impacts was not investigated nor mentioned. They reported motion of the state of polarization of 45000 kRot/s.

Their work was extended by Boroditsky et al who measured high speed polarization changes in installed fibres. They observed the state of polarization in a 40km fibre link, and recorded any polarization changed more than five degrees within 10ms. They reported that some fast polarization effects in installed fibre optic systems were elastic[3], which means that the light quickly returns to its initial SOP state following a disturbance. Their measurement rate was only 50 kHz so they were unable to observe these fast polarization effect in detail.

In this thesis, we will examine polarization fluctuations generated by carefully

controlled impacts on DCMs. We find, to our knowledge for the first time, that such mechanical impacts also generate elastic changes in the SOP. Thus consecutive impact measurements can be performed on the same initial state of the DCM. From this we have been able to demonstrate the repeatability of polarization fluctuation due to controlled impacts. This enables the characterization of transient polarization properties that normally cannot be reliably measured.

1.6 Conclusions

In this chapter, we have discussed the elements of an optical communications network with emphasis on the polarization properties that contribute to or degrade its efficient and reliable operation. We observed that dispersion compensating modules are integral to the optical network structure, and that high-speed state of polarization changes are therefore detrimental to network performance. We also surveyed prior work in the area of this thesis. We concluded with our major achievements; the discovery that polarization fluctuations due to mechanical impacts on DCMs are repeatable between successive impacts as a result of the elastic response of the DCM to deformations.

The second chapter will introduce the methods that we employed to measure fast changes in the state of polarization generated by physical impacts on dispersion compensating modules. In the third chapter we develop our experimental results for the fast changes in polarization resulting from these impacts and the possible influence on the reliable transfer of data through an optical system that is influenced by such disturbances. The fourth chapter extends our results by presenting a mathematical formalism based on polarization rotation vectors. Finally, in the fifth chapter we discuss applications of our experimental methods based on the repeatability of polarization evolution during successive experiments.

Chapter 2

Measurements

This chapter presents methods for measuring the state of polarization at the output of dispersion compensating modules during high-speed oscillations created by an impact force. First we discuss the equipment employed in the experiment. Secondly the procedures employed to create repeatable impact forces as well as to compare the effects of separate impacts will be summarized.

2.1 Experimental Technique

2.1.1 Commerical Polarimeters

Numerous commercially available polarimeters can be employed to determine the SOP of a light source. We in particular employ an HP8509B, which was designed for low speed PMD measurements as a calibration device. While the HP8509B easily determines the SOP, the sampling speed is limited to approximately 2000 data points per second. High-speed polarimeters are now available at sampling rates of up to 1MHz, but these are expensive and complex.

2.1.2 Measuring Polarization

A measurement of the state of polarization of light requires the determination of four different components. This can be achieved in many different ways. One set of procedures employs a single photodetector, a polarizer and retardation plate. The polarizer and retardation plate are placed in the path of the laser before the

photodetector and are rotated to change the light polarization received by the photodetector. The state of polarization is then calculated from the intensity of the light received as a function of the angles relative to the laboratory axis of the polarizer and plates. Another group of methods splits the light into four paths, each with a separate set of fixed optical elements, and the intensity of the light after each path is recorded continuously with a separate photodetector[2]. Such techniques do not require physical movement of the optical elements and therefore enable shorter measurement times as well as simultaneous measurements of the different polarization components as their speed is only limited by the photodetectors and the sampling rate of the electronics. On the other hand, the first group of methods require fewer optical elements and are therefore simpler and less expensive to construct (although the adjustable optical elements somewhat increase the complexity of the apparatus).

Since we require small measurement times, we followed the concepts of the second set of measurement techniques in which our four paths measured the total power, horizontal linear power, 45 degree linear power, and left-hand circular power. The stokes parameters were then obtained from these power values according to (Eq. 2.1).

$$\begin{aligned} S0 &= P_{\text{tot}} \\ S1 &= 2P_{\text{hlp}} - P_{\text{tot}} \\ S2 &= 2P_{\text{45p}} - P_{\text{tot}} \\ S3 &= 2P_{\text{lcp}} - P_{\text{tot}} \end{aligned} \tag{2.1}$$

in which P_{tot} is the total measured power and $P_{\text{hlp}}, P_{\text{45p}}, P_{\text{lcp}}$ are the power measurements from horizontal linear polarization, 45 degree linear polarization and left-hand circular polarization respectively.

2.1.3 Polarimeter Design

To construct a high-speed polarimeter according to the second method of the previous section we first employed a 4x1 optical fibre power splitter at the input, and connected one of the output fibres directly to a photodiode. Along each of the other three paths a manual polarization controller is followed by a linear polarizer and subsequently a photodiode according to the design of Fig. 2.1. The polarimeter requires a calibration step that aligns the manual polarization controllers. A

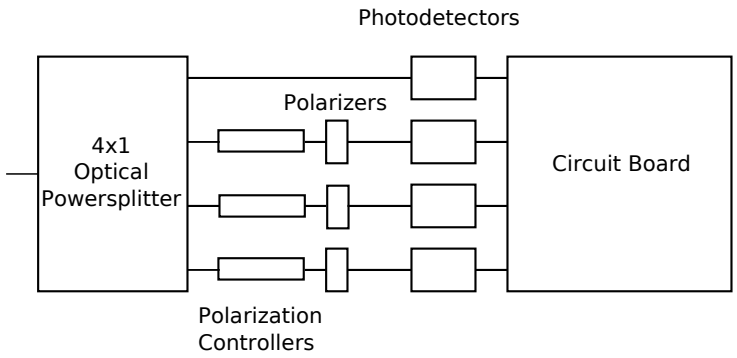

Figure 2.1: Schematic diagram of high-speed polarimeter

95%-5% optical fibre power splitter was employed before the polarimeter with the 95% branch routed to the polarimeter while the polarization of the light in the 5% branch was monitored with a commercial HP8509B polarimeter. A polarization controller at the output of the laser was employed to vary the input polarization. We accordingly generated three orthogonal input polarizations in sequence and adjusted the controller to minimize the power on one independent path for each of the three input polarizations. The power tap connected to the HP8509B was then employed to compare the polarization measurement of the HP8509B with those of our polarimeter setup. Here we performed simultaneous measurements with both the HP8509B and our polarimeter for 100 different input polarizations. Then from a least squares fit to these measurements, we generated a matrix which translates the voltages from the polarimeter to the corresponding stokes parameters values that were obtained from the HP8509B. Subsequently, this calibration matrix was employed to translate the measured voltages from the polarimeter to Stokes parameters.

2.1.4 Data Collection

We recorded data by connecting the output of the photodiodes through a transimpedance amplifier circuit to a PC analog input data acquisition card. We developed a MATLAB program to read in and process the voltage data from the input card. The program then estimated the Stokes parameters from the calibration matrix of the preceding section. We found here that the HP8509B and the high-speed polarimeter measurements differed by less than 0.22 degrees over 200 measurements[22]. The standard deviation was $\approx 0.05^\circ$ and the mean error was $\approx 0.07^\circ$. Since the analog input card has a sampling frequency of 250,000 samples

per second, we could measure changes in the state of polarization much more rapidly than possible with commercial equipment, such as the HP8509B which is limited to 2000 samples per second[1]. We further acquired a high-speed digital oscilloscope that increased the rate at which the state of polarization could be sampled to 50 million samples per second. Since this oscilloscope however can only store 120,000 samples in memory, most measurements were performed at a sampling rate of 2.5 or 5.0 million samples per second. This allowed the SOP to be measured for 24 or 48 ms, and provided a sufficiently high sampling rate for the impacts of interest.

2.1.5 Dispersion Compensating Module Impact Measurements

To observe rapid polarization changes, we inserted light from a continuous wave laser into a dispersion compensating module and then into our high-speed polarimeter. When a small impact was applied to the DCM, by manually striking the DCM with a hex screwdriver, the output of the polarimeter revealed that the polarization described numerous rapid rotations around the Poincaré sphere that could not be resolved by the HP8509B (Fig. 2.2). Fig. 2.3 illustrates this by displaying the Stokes parameters during an impact as recorded by both the high-speed polarimeter and the HP8509B. Clearly only our new polarimeter can record the rapid polarization activity of the DCM that rapidly decreases in amplitude and frequency as the SOP returns to its position prior to impact(Fig. 2.4).This confirms that an impact on a DCM creates an "elastic" SOP change as observed by Boroditsky et al[3] during measurements of installed fibre optic systems.

In this study we examined the effect of impacts on four different DCMs. The first DCM was produced by Avanex, and is therefore referred to here as the Avanex DCM. This DCM contained approximately three kilometres of DCF wrapped around a circular metal core and secured in place with epoxy covering the outer layer of fibre. The second DCM was sourced from Nortel, and contained approximately twelve kilometres of DCF wrapped around a circular metal core and secured in place with vertical strips of epoxy. The third and fourth DCMs were also produced by Nortel but were of a different design. The DSCM10 had around one and a half kilometres and the DSCM20 had three kilometres of DCF wrapped around a circular metal core and secured with vertical strips of epoxy. The numbers 10 and 20 in the model names refer to the length of standard fibre (in kilometres), for which the DCMs are designed to compensate the chromatic dispersion.

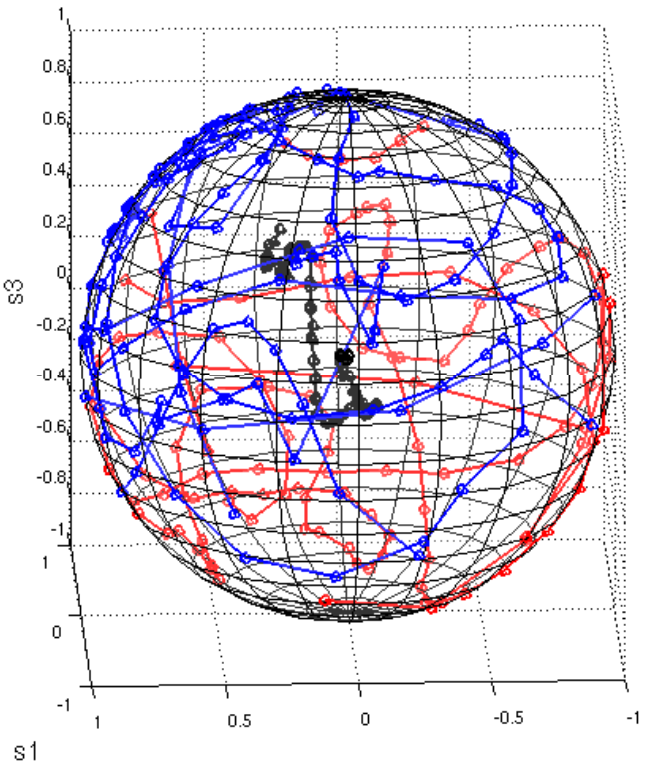

Figure 2.2: A comparison of the evolution of the polarization state on the Poincaré sphere with time after an impact on a Nortel DCM as recorded by an HP8509B (black lines) and by our high-speed polarimeter (blue on near side of sphere and red on the far side of sphere)

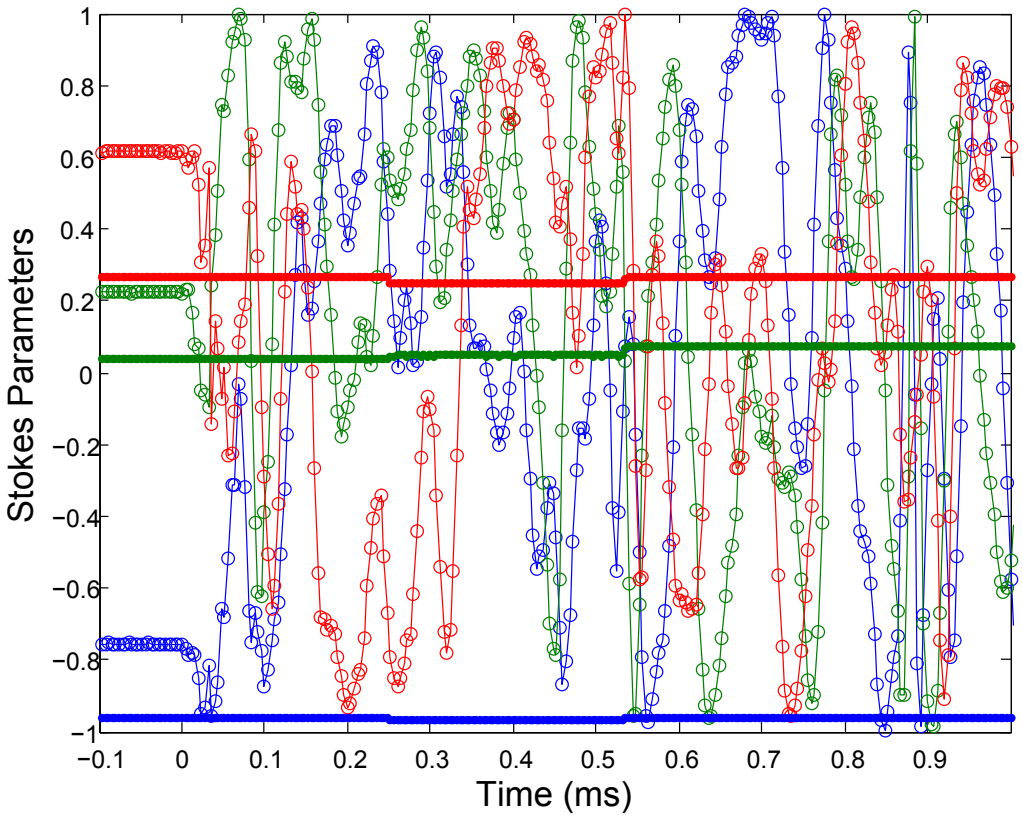

Figure 2.3: The Stokes parameters as simultaneously measured by the HP8509B (dots) and our high-speed polarimeter (open circles) during an impact on the Nortel DCM (Red s1,Blue s2,Green s3)

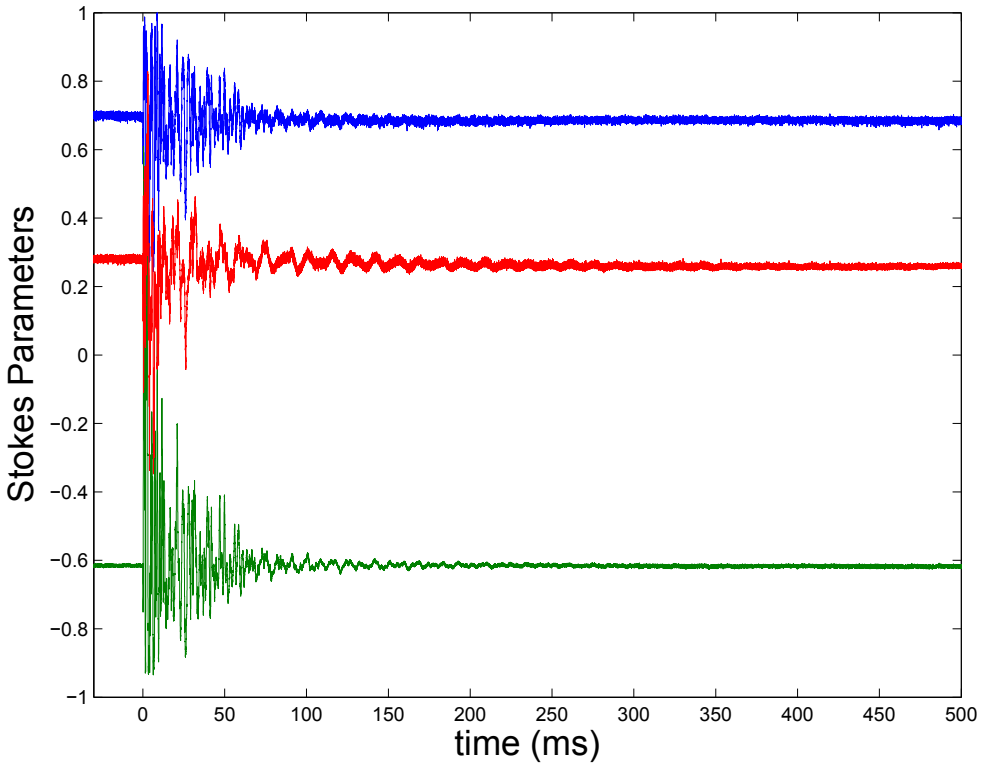

Figure 2.4: Stokes Parameters vs Time for Impact on Avanex DCM

2.2 Repeatable Measurements

2.2.1 Repeatable Ball Drop Device

In order to more rigorously investigate the changes in the state of polarization from physical impacts on the DCM we require a method for generating reproducible impact forces. Accordingly, we designed an electromagnetic mechanism which precisely released a steel ball from a fixed but adjustable position such that the impact point for a group of impacts was within one millimetre of the mean impact point. For the resulting impact force to be repeatable to within our specifications, after numerous attempts we chose the design of Fig. 2.5. The ball release mechanism consisted of a steel ball fastened to an optical table screw with magnet wire wrapped around the screw to form the electromagnet. The wire was connected through a switch to a power supply via a current control circuit, and the electromagnet was held in place above the DCM with optical table posts. In this manner, the electromagnet could be easily positioned at any given height above the DCM and tightened so that it would remain in position throughout the series of measurements. An image of the setup is shown in Fig. 2.6

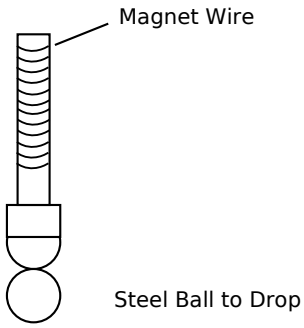

Figure 2.5: Diagram of the electromagnet employed in the ball release mechanism

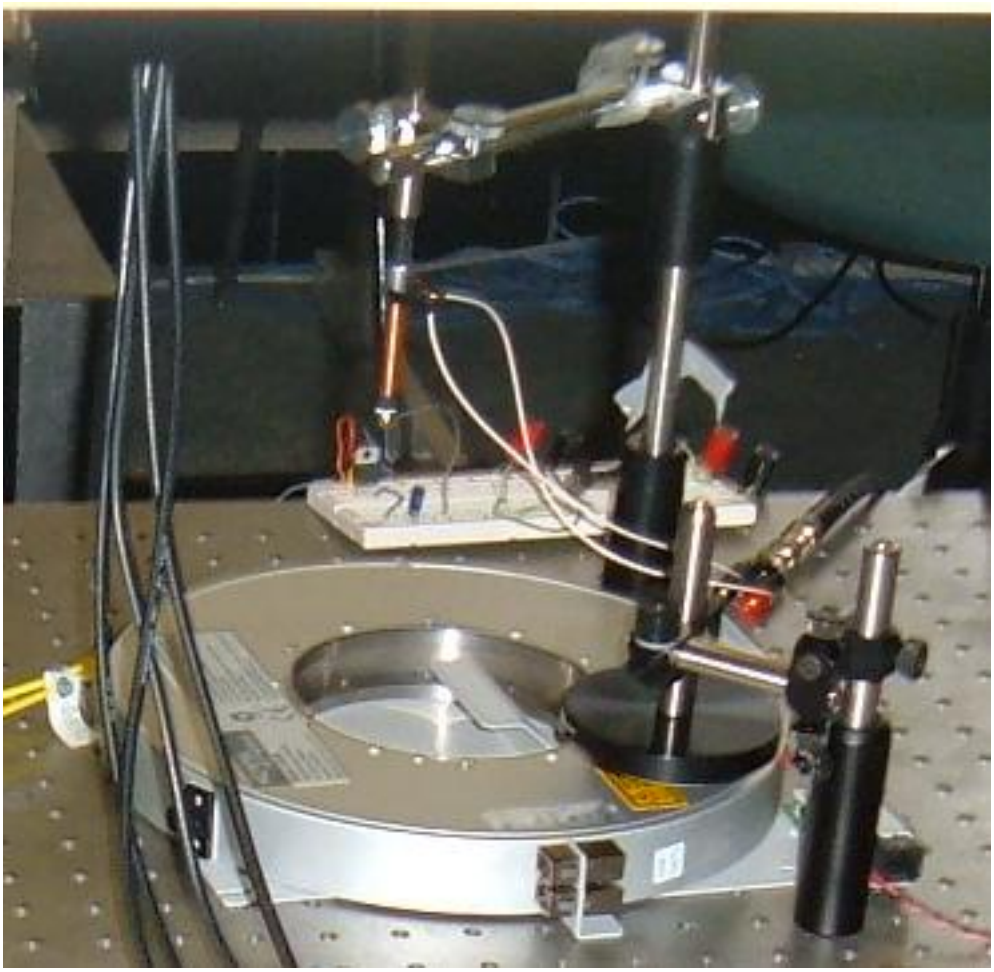

Figure 2.6: Image of the ball release mechanism

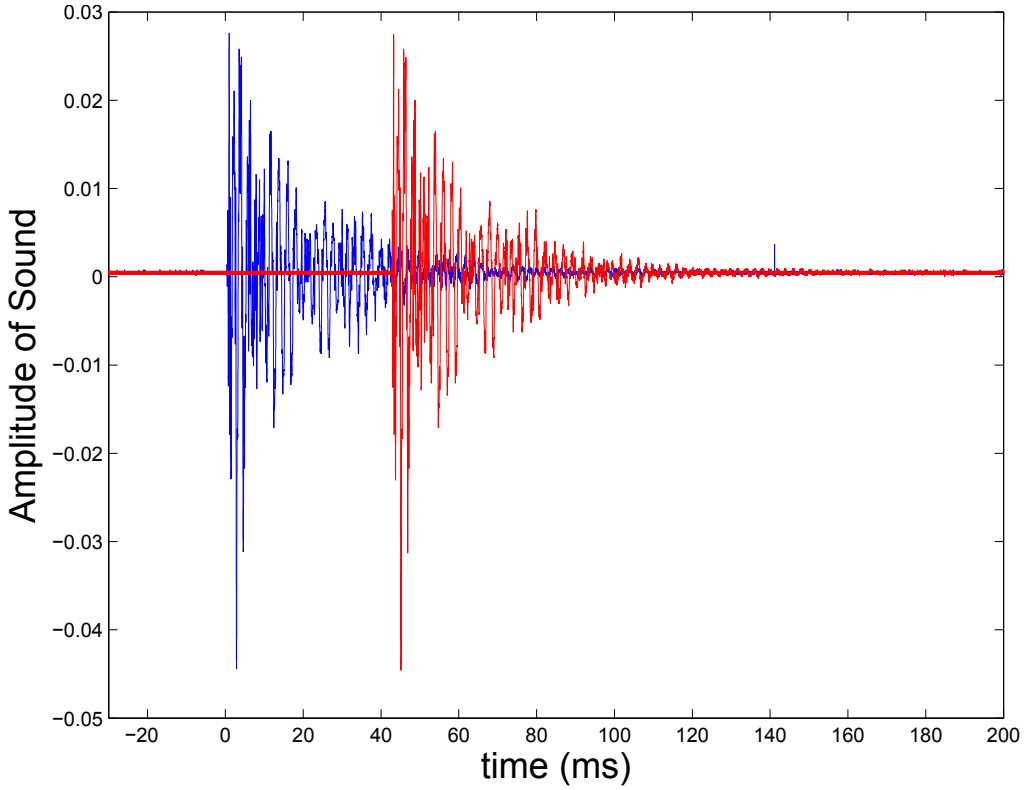

Figure 2.7: The sound wave generated by two impacts. The offset between the two sets of measurements is employed to align the polarization data.

2.2.2 Multiple Time Series Comparison

To compare the polarization traces of multiple impacts with the same or different input polarizations as a function of time, the starting time of all measurements in the series has to be aligned with a degree of precision that is dependent on the timescale of the polarization fluctuations. Simply employing a voltage-controlled switch triggered by our computer program yielded uncontrollable, varying time delays between the time that the ball was released under software control and the beginning of the recorded data sequence. Instead, we simply employed the audio signal recorded with a microphone after impact to align the time series. The audio data was collected with the same analog input card as the photodetector voltages. This eliminated any potential timing difference between the acoustic and optical signals from each measurement. We found that the acoustic waveforms were identical for any two impacts of the same position and height while the recorded time offset between any two sound waves coincided with the offset between the respective polarization data, as illustrated in Fig. 2.7. Such measurements justify our employing sound data to align the time of impact in each data set.

2.2.3 Signal Repeatability

Once we could create a repeatable impact and were able to align the time series arising from successive drops, we could analyze the polarization effects generated by a given impact in detail. Here we found by repeatedly measuring the polarization evolution of many identical impacts that the recorded time evolution of the state of polarization of the impacts was nearly identical among different ball drops. The time between impacts must be large enough for mechanical equilibrium to be restored. We consider the time at which equilibrium is attained to be the point at which the SOP returns to the initial position so that the change in measured SOP is dominated by measurement noise. This time, which depends on the impact and the DCM, was found to be ≈500ms for the Avanex DCM and ≈10s for the Nortel DCM. However, the equilibrium SOP of the DCM varies on the order of 10 degrees per hour as a result to environmental factors.

Fig. 2.8 displays the recorded SOP evolution for multiple drops registered within a 5 minute time interval. As we will demonstrate in the next chapters, the repeatability of our impact measurements enables the analysis of polarization effects that could not normally be examined at such high speeds. In particular, we measure quantities which require repeated measurements at different wavelengths and input polarization states such as the PMD. Of course our measurement flexibility is limited by slowly changing but difficult to control environmental effects, in particular ambient temperature changes.

2.3 Conclusions

We have discussed the design of a high-speed polarimeter that we have employed to measure the changes in the polarization state after a carefully controlled mechanical impact on a dispersion compensating module. In particular, we have demonstrated that these transient responses, while very rapid, are identical among successive impacts if sufficient care is taken to create highly repeatable impact forces. Through a simple yet accurate procedure, we were able to generate such impacts through an optimized electromagnetic ball release mechanism, and a stable triggering source. The reproducibility of these measurements, which we were the first to observe, enables the determination of the full time-dependent trajectory of the polarization in the two subsequent chapters.

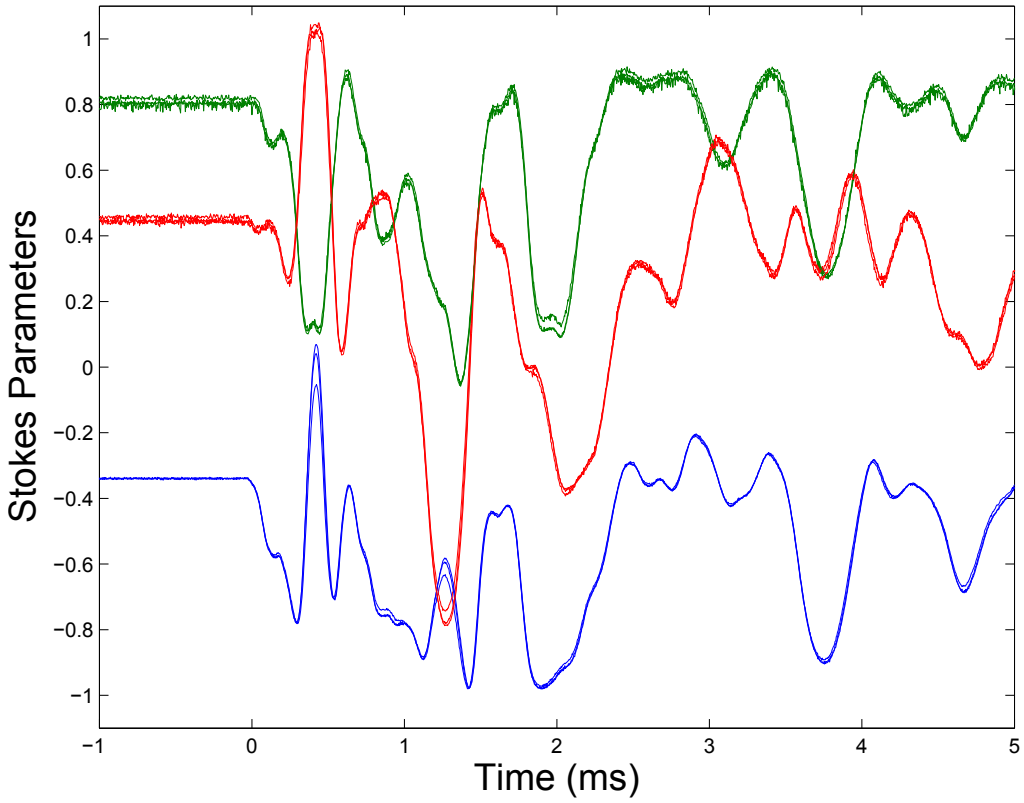

Figure 2.8: The state of polarization as a function of time after three impacts on a DCM.

Chapter 3

Analysis

We now examine the change in the state of polarization induced by mechanical impacts as measured with the apparatus of the previous chapter. We examine in particular the velocity of the SOP on the Poincaré sphere and its local behaviour but will also investigate further the repeatability of the SOP trace for consecutive identical impacts on the dispersion compensating module.

3.1 Rotation of SOP during Impact

3.1.1 SOP Evolution

The time evolution of the output state of polarization from a DCM after an impact on the DCM follows certain deterministic patterns. Thus immediately after impact the motion is dominated by large nearly uniform arcs on the sphere in many measurements. This can be clearly seen in Fig. 3.1 which depicts the SOP evolution on the Poincaré sphere for the first 100 μs after a Nortel DCM is impacted with a half inch steel ball from a height of 11cm.

3.1.2 SOP velocity

Perhaps the simplest measure of the polarization change is provided by the speed of the polarization vector on the Poincaré sphere. The speed of the SOP is calculated from the angular separation between two measurements separated by a time interval Δt (Eq. 3.1). From these values, $v_{\mathrm{sop}}(t)$, the SOP change in radians per millisecond, is obtained from (Eq. 3.2).

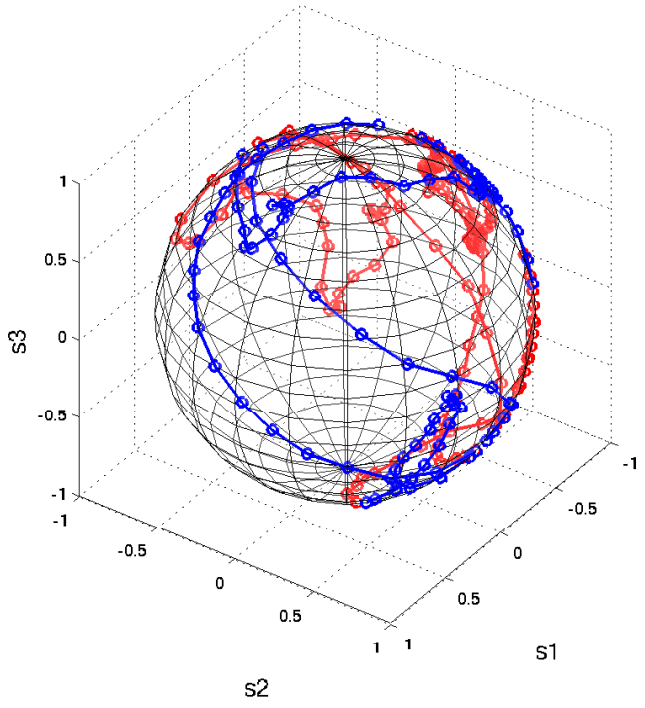

Figure 3.1: The SOP on the Poincaré sphere during the first 100μs after impact. The blue and red lines and circles are the SOP on the near side and far sides of the sphere respectively. The circles indicate the actual measurements spaced by 400 ns while lines connect consecutive measurements.

$$\theta(t, \Delta t) = \arccos\left(\hat{s}(t) \cdot \hat{s}(t - \Delta t)\right) \tag{3.1}$$

$$v_{\text{sop}}(t) = \frac{\theta(t, \Delta t)}{\Delta t} \tag{3.2}$$

(Eq. 3.1) then yields

$$\theta(t, \Delta t) = \arccos\left(1 - \frac{1}{2}\Delta s^2\right) \tag{3.3}$$

in which $\Delta s \equiv |\hat{s}(t) - \hat{s}(t - \Delta t)|$.

Fig. 3.2 displays the speed of the change of the state of polarization as a function of time for the single impact considered in Fig. 3.4. The SOP fluctuations observed for low velocities results in large part from measurement noise. In these regions the change in SOP is small due to the high measurement rate, while the noise level remains constant. To calculate $v_{\text{sop}}(t)$ accurately in both the low and high velocity regions Δt was increased at lower speeds to preserve the signal to noise ratio. Isolating the noise term from the $\hat{s}$ term, we can transform (Eq. 3.3) into

$$\theta(t, \Delta t) = \arccos\left(1 - \frac{1}{2}\left((\Delta\hat{p})^2 + 2\cos(\phi)\Delta\hat{p}\Delta n + (\Delta n)^2\right)\right) \tag{3.4}$$

Here $\hat{s} = \hat{p} + n$, $\hat{p}$ is the state of polarization without noise and n is the noise. $\Delta\hat{p}$ is the difference between $\hat{p}(t)$ and $\hat{p}(t - \Delta t)$. Δn is the difference between $n(t)$ and $n(t - \Delta t)$. In most cases $\Delta\hat{p}$ grows monotonically with Δt while ϕ and Δn are independent of Δt. Therefore, increasing Δt yields a larger signal to noise ratio as expected. Since the velocity of the SOP varies with time, augmenting Δt decreases the precision of the local measured value of the velocity. In the extreme case that Δt is chosen to be excessively large, the SOP traverses an angle greater than π radians and the angular displacement becomes ambiguous. Therefore we select the smallest possible value of Δt for each time t subject to the condition that Δs is above the noise floor.

In Fig. 3.2, random angular variations of up to 0.05 radians are associated with the measurement noise. The angular speed of the SOP was calculated at each time t with the smallest Δt value for which angular change $\theta(t, \Delta t) > 0.05$ radians. Fig. 3.2 then indicates that the angular speed of the SOP reaches a maximum just after impact after which it rapidly decreases toward zero.

Table 3.1 indicates the maximum speed as a function of release height of the ball for two different dispersion compensating modules. The average speed of the

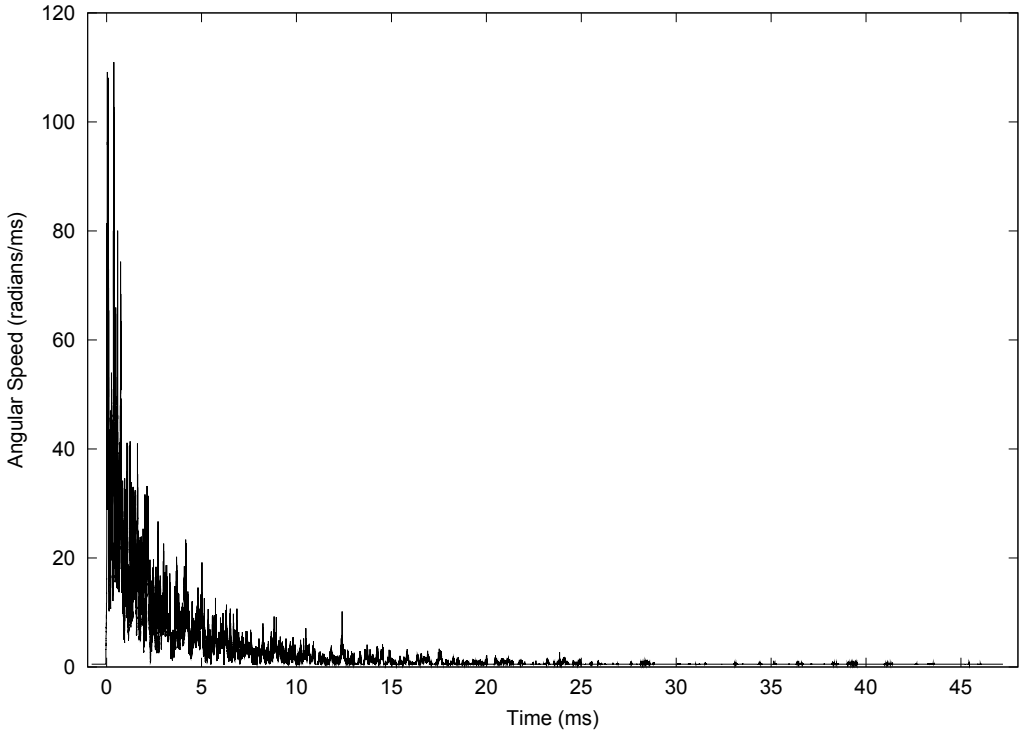

Figure 3.2: Time variation of the SOP after impact

Table 3.1: Maximum Velocity of SOP on Poincaré sphere

Avanex DCM		Nortel DCM	
Height	Arc Velocity (radians/ms)	Height	Arc Velocity (radians/ms)
5cm	73.861	5cm	606.008
7cm	101.521	7cm	791.450
9cm	106.439	9cm	799.637
11cm	110.982	11cm	1052.642

SOP varies similarly with release height for these DCMs as evident from table 3.2. For both DCMs the maximum and average speed of the SOP increases with the release height. A one half inch diameter steel ball dropped onto the Nortel DCM from a height of 5 cm induces rotations in the state of polarization of 90 kRot/s while a release height of 11 cm yields rotations of up to 180 kRot/s, which is four times as fast as the rotations reported by Krummrich and Kotteo [17]. Clearly the design of a DCM greatly influences its response to mechanical impacts.

Table 3.2: Average velocity of SOP on Poincaré sphere during the first 40 ms after impact

Avanex DCM		Nortel DCM	
Height	Arc Velocity (radians/ms)	Height	Arc Velocity (radians/ms)
5cm	1.7111	5cm	4.3785
7cm	2.0101	7cm	4.9346
9cm	2.2933	9cm	5.4427
11cm	2.5762	11cm	6.0902

3.2 Measurement Repeatability

As noted above, our ball drop mechanism yields repeatable impacts.

However, to quantify the degree of repeatability, we compare the angular separation, $\theta_{\text{sep}}(t)$, between the recorded SOP traces of two successive impacts at each time t as calculated with (Eq . 3.5).

$$\theta_{\text{sep}}(t) = \arccos\left(\hat{s}_1(t) \cdot \hat{s}_2(t)\right) \tag{3.5}$$

where the subscripts on $\hat{s}$ refer to the number of the measurement. We can further compare this angular separation to the angular noise calculated from the SOP data recorded before the actual impact (i.e. for $t < 0$). This noise is defined as the difference between the measured SOP at time $t < 0$ and the mean measured SOP for all time $t < 0$ (Eq. 3.6).

$$\theta_{\text{noise}}(t) = \arccos\left(\hat{s}(t) \cdot \overline{\hat{s}}\right) \tag{3.6}$$

If the distribution of angular separations between the SOP for two impacts coincides with the distribution of angular noise, the SOP traces can be considered identical. As a result of the discrete nature of the recorded data, the two data records can be misaligned by a time as large as Δt; that is, the assumed impact time can be any value within the interval $t = -\Delta t/2$ and $t = \Delta t/2$. Fig. 3.3 illustrates this effect of discrete sampling using a simulation of data sampling. For two measurements, if for the first measurement the sample at time slot zero happens to be measured at $t = \tau_1$ and the second at $t = \tau_2$, in the absence of noise the difference in SOP at any time t will be the distance in SOP travelled between $t+\tau_1$ and $t+\tau_2$. As a result, for high velocity SOP changes the angular difference associated with alignment errors can exceed the angular noise.

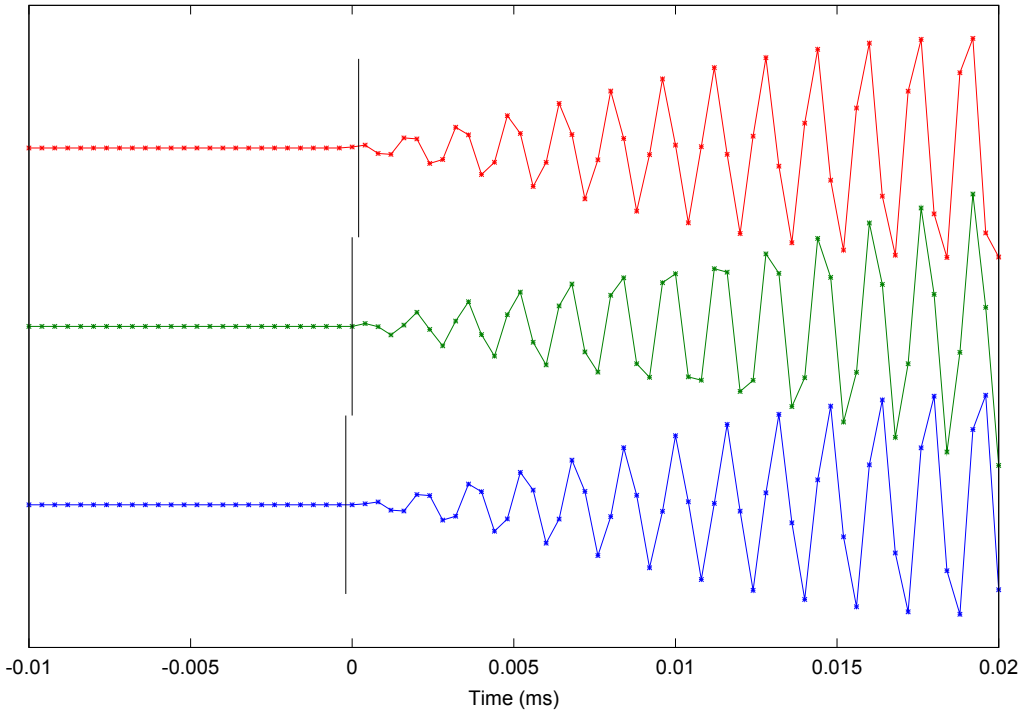

Figure 3.3: Illustration of the effect of the discrete data sampling rate on measured data, where the green, red and blue stars are the sampled data for the same function. The black lines are the true $t = 0$ value for the function.

To quantify these effects, the angular difference associated with the SOP velocity is given by

$$\theta_{\text{vel}} = \arccos\left(\hat{p}_1(t) \cdot \hat{p}_2(t)\right) \tag{3.7}$$

while for two impacts with identical SOP the angular difference θ_{vel} resulting from the misalignment within an interval δt is

$$\theta_{\text{vel}} = \arccos\left(\hat{p}_1(t) \cdot \hat{p}_1(t + \delta t)\right) \tag{3.8}$$

The angle between $\hat{p}_1(t)$ and $\hat{p}_1(t + \delta t)$ approximately equals the angular velocity at time t multiplied by δt.

$$\theta_{\text{vel}} \approx v_{\text{sop}} \delta t \leq v_{\text{sop}} \Delta t \tag{3.9}$$

When $v_{\text{sop}}\delta t$ is large, the measured angular difference between two identical SOP can significantly exceed the angular noise and the two SOP values cannot be reliably compared. Increasing the sampling rate decreases both Δt and the possible misalignment range δt, insuring that $v_{\text{sop}}\delta t$ remains lower than the angular noise.

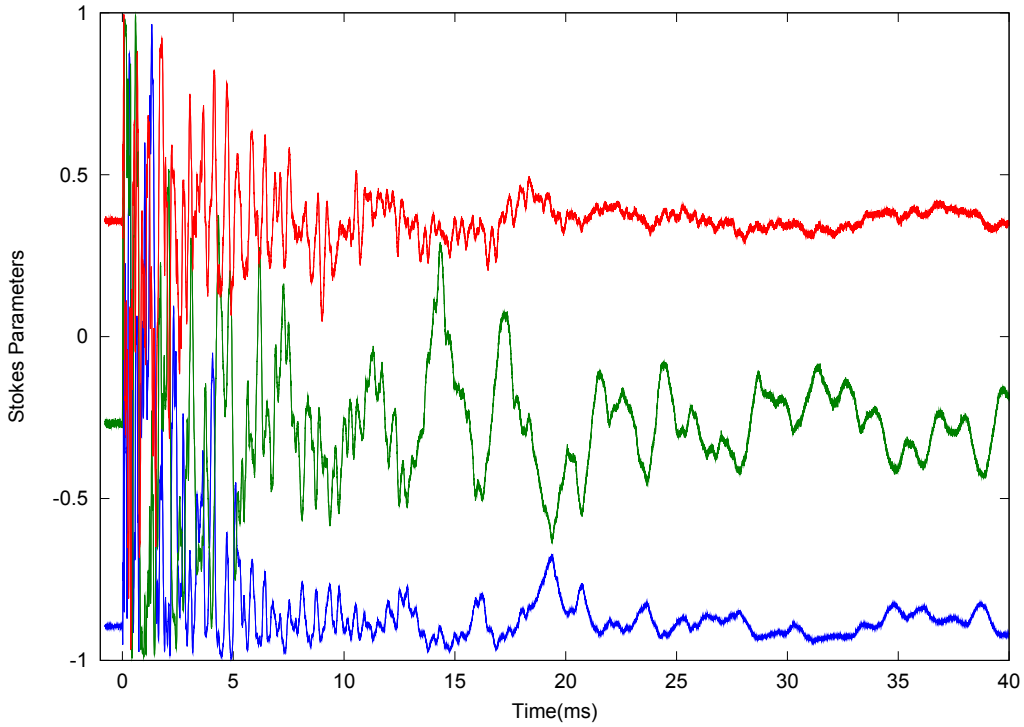

Figure 3.4: The time evolution of the Stokes parameters for two impact events with 11cm release heights for the Avanex DCM

3.2.1 Avanex DCM Repeatability

The repeatability of the SOP measurements for identical impacts was first tested with an Avanex DCM. The SOP was measured for two identical ball drop heights, cf. Fig. 3.4. The angular noise was calculated from the measured SOP during the pre-impact time of the first ball drop. The angular difference between the two SOP measurements for each time t was then evaluated, cf. Fig. 3.6. The angular speed as a function of time was generated with the procedure in Section 3.1.2. Finally, Fig. 3.5 displays the cumulative distribution function for the angular noise as well as the angular difference between SOPs. The cumulative distribution function of x is the probability that the angular separation is less than x. The similarity between the distributions of the angular noise and the angular differences demonstrates that the two impacts yielded nearly identical SOP traces as functions of time.

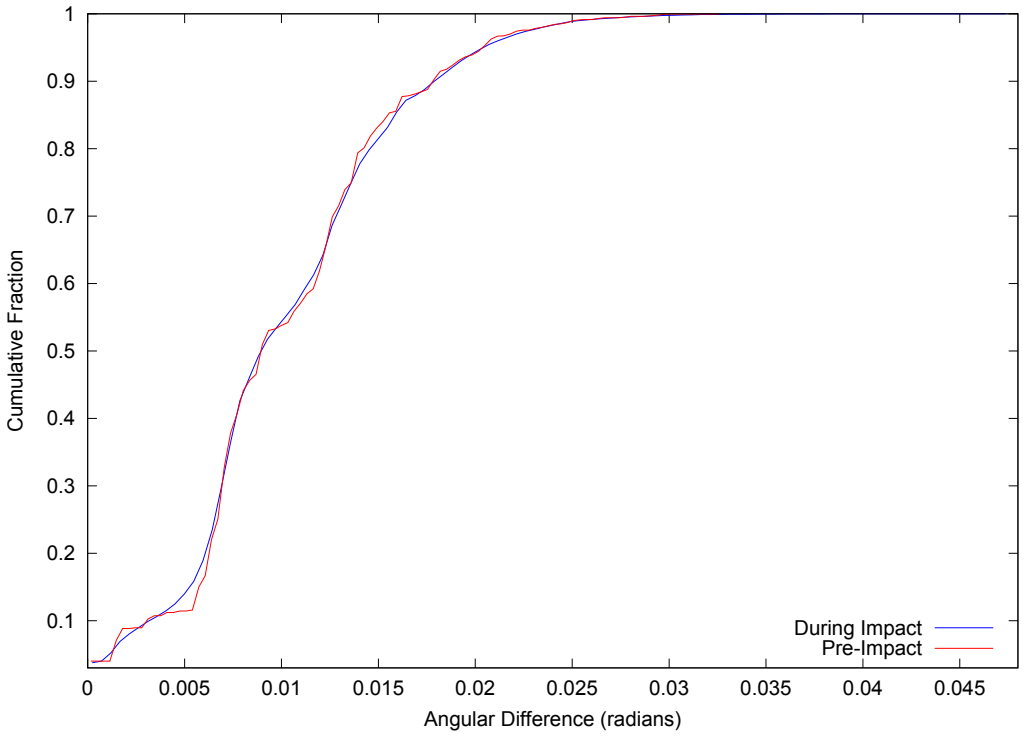

Figure 3.5: The cumulative distribution function of the pre-impact angular noise and the angular difference in SOP between two impacts

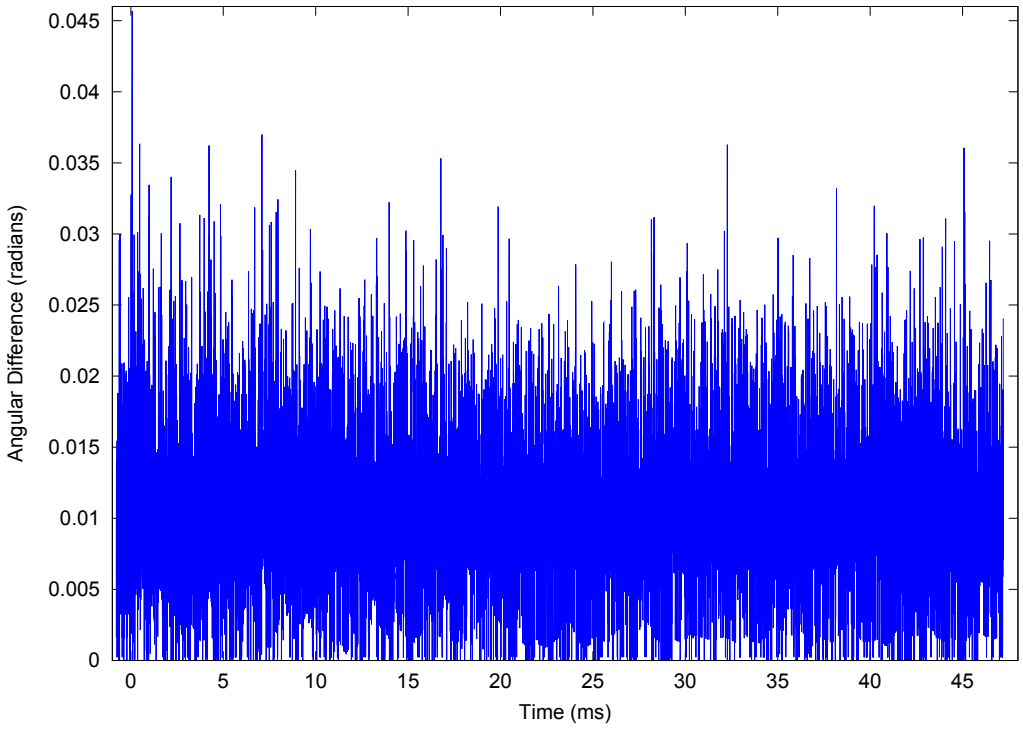

Figure 3.6: The angular difference between the SOP of two impacts

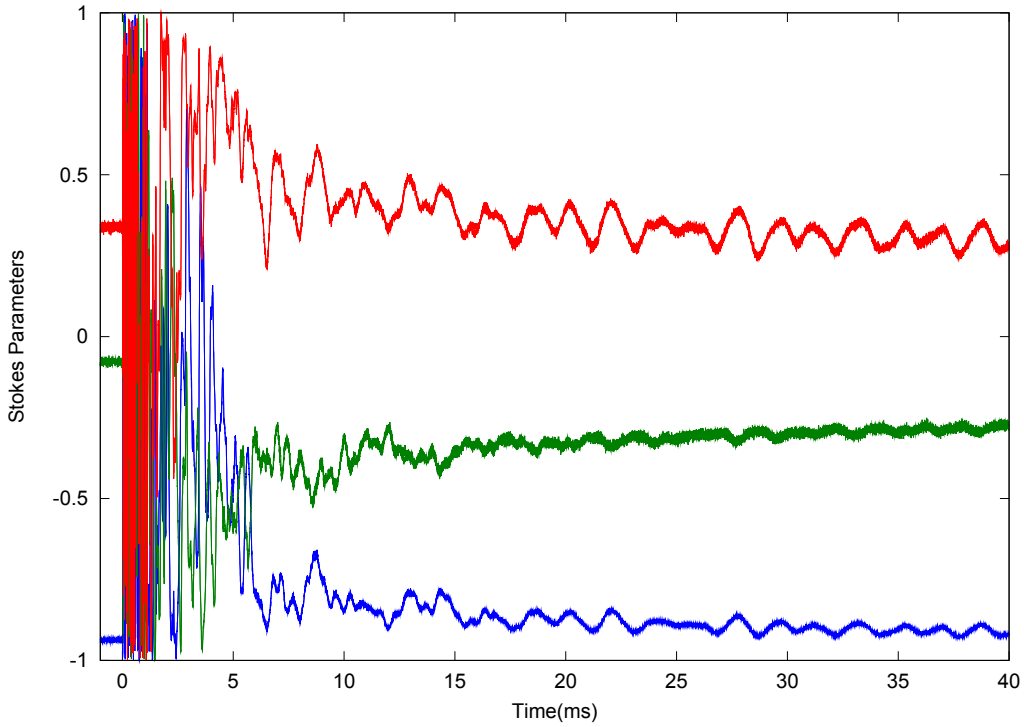

Figure 3.7: Stokes parameters as a function of time for two impact events with a 11cm release height onto the Nortel DCM

3.2.2 Nortel DCM Repeatability

We have also examined the repeatability of the SOP time evolution after mechanical impacts on a Nortel DCM. Here we again measured the SOP for two identical ball release heights (Fig. 3.7) in which the angular noise and angular velocity of the polarization were respectively evaluated from the SOP during preimpact and the method of Section 3.1.2. The angular difference between the two SOP measurements is displayed in Fig. 3.9 while Fig. 3.8 displays the cumulative distribution function for the angular noise, and the angular difference between SOPs. Note that these latter distributions indicate that some SOP points possess a larger angular difference than that generated by the noise contributions. Comparing the angular velocity in Fig. 3.10 to the angular difference as functions of time (Fig. 3.9) demonstrates that large SOP angular speeds correspond to large angular differences between measurements.

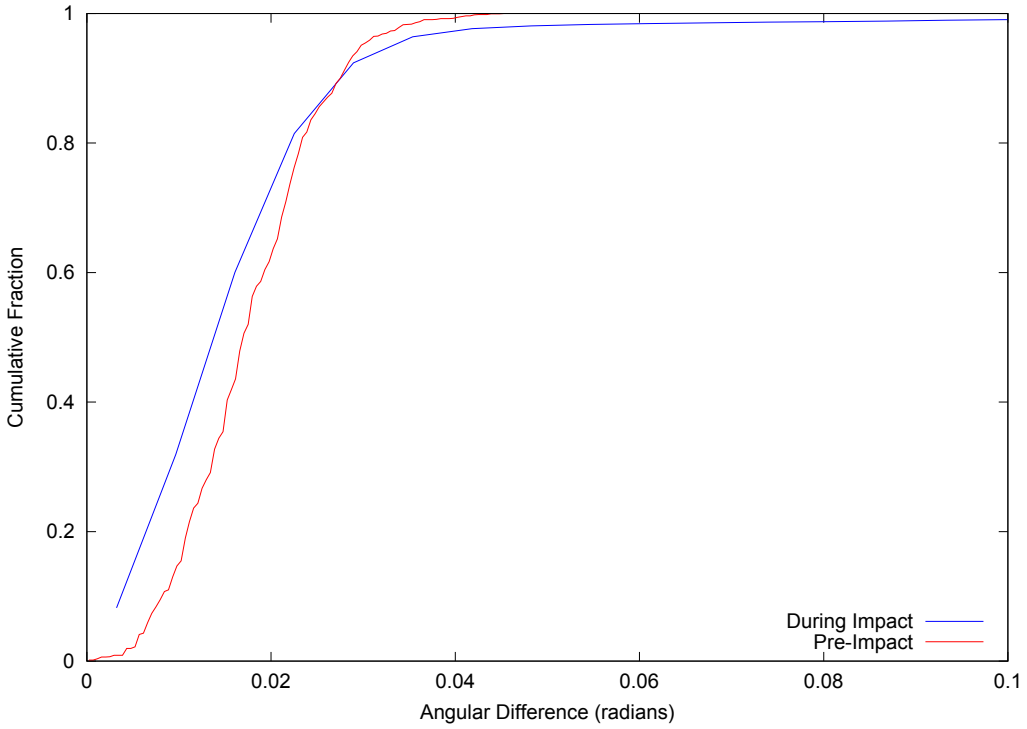

Figure 3.8: Cumulative distribution function of the angular noise before impact and the angular difference in SOP between two impacts

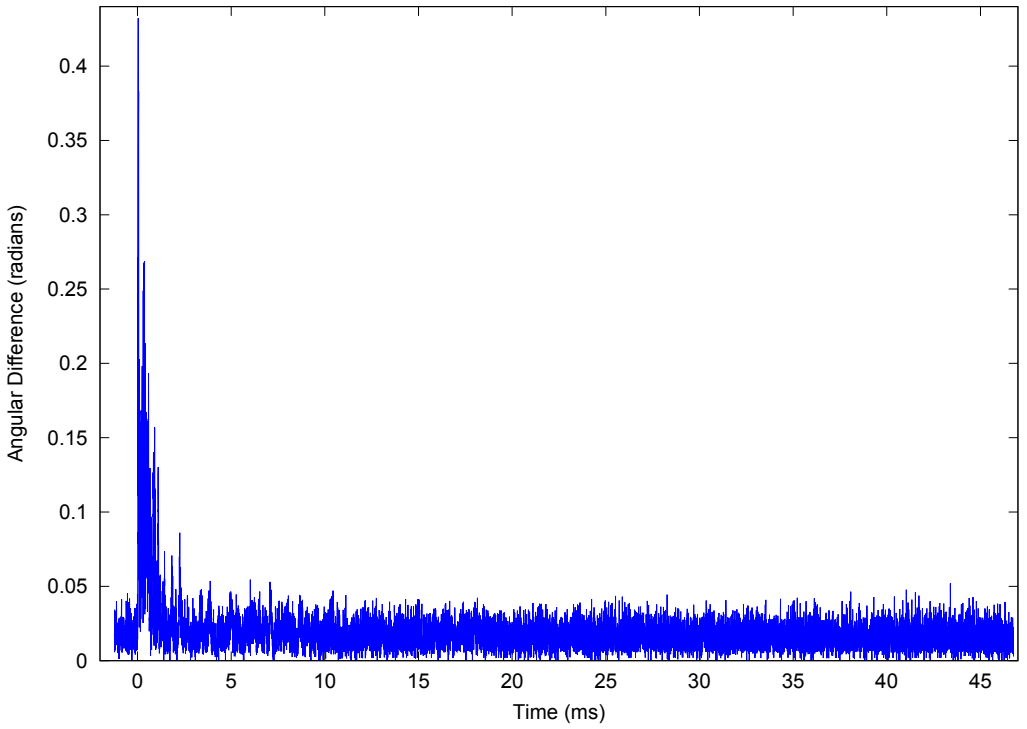

Figure 3.9: The angular difference between the SOP for two impacts

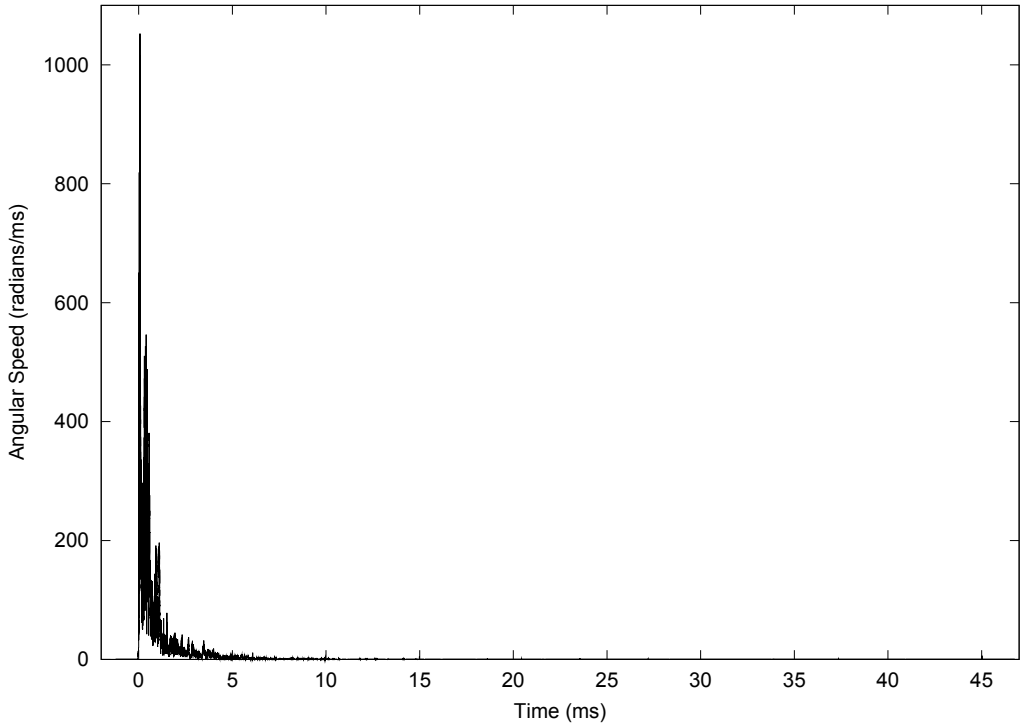

Figure 3.10: The angular speed of the SOP for an 11cm release height

3.3 Conclusion

In our analysis of the polarization evolution after mechanical impacts on a dispersion compensating module, we have observed a higher speed for the polarization change than reported previously. Furthermore, we have demonstrated that the manner in which the DCM is manufactured greatly affects the nature of the polarization oscillations. We have also quantified the degree to which the oscillation from a controlled impact is the same for successive impacts. This result, which has not be reported previously, can be employed to determine numerous polarization dependent physical quantities as will be detailed in subsequent chapters.

Chapter 4

Numerical Analysis

In the previous chapter we demonstrated that successive controlled mechanical impacts yield the same polarization response for a DCM. We now examine the manner in which data from successive impacts with different input polarizations can be combined to generate a comprehensive time dependent model of the polarization rotation vector that characterizes the impact at a single wavelength. These rotation vectors will then be analyzed to quantify the frequencies generated by the impact. Similar measurements at different wavelengths can also be employed to quantify more complex quantities such as different orders of the PMD.

4.1 Rotation Vectors

A rotation in a three dimensional space moves points along circles centred on and perpendicular to a given axis. The angle around the circle travelled by each point is the angle of rotation. The direction of a positive rotation is determined by the direction of the axis and the right-hand rule. The rotation can be represented by a three dimensional rotation vector, for which the magnitude is the angle of rotation and the axis of rotation coincides with the vector direction. The rotation can further be represented by a matrix such that a rotated vector is simply the rotation matrix times the initial vector.

Any two points on a unit sphere can be connected by a group of rotations. The axes of the rotations in the group are all co-planar. This plane bisects the two points and is at right angles to the line connecting the two points. The angle of rotation associated with each axis varies with their position. If a second set of

points can be connected by the same rotation as the first set the axis and angle will both match at two antipodal points.

The time-dependent rotation of the polarization cannot be extracted from a single measurement with a single input SOP. Rather, each input SOP yields one set of points at each time t, the initial SOP and the SOP at time t. Therefore to define the rotation uniquely at each time t at least two measurements are required. For points that are close to the axis of rotation, the errors in the rotation axis and angle principally result from the influence of the measurement noise on the recorded SOP value. Therefore we have employed four or more sets of initial polarizations that are randomly distributed around the Poincaré sphere, as described below.

4.1.1 Measurements

The repeatability among measurements discussed in the previous chapter can be employed to perform measurements of the optical response to the same excitation for multiple input polarizations simply by changing the input polarization between identical impacts. Thus, to determine the rotation vector, a ball is released from a specified height and the polarization is recorded as a function of time. This measurement is then repeated with the input polarization controller set to a new polarization. After two or more measurements of the output SOP with different input polarizations are recorded, the time dependent rotation matrix can be calculated using the SVD method [15] (Eq. 4.4) for each time t. The best fit rotation matrix $\mathbf{R}(t)$ will minimize

$$\sum_{\alpha=1}^{N} ||\hat{s}_\alpha(t) - \mathbf{R}(t)\hat{s}_\alpha(t=0)||^2 \tag{4.1}$$

where $\hat{s}_\alpha$ is the SOP vector of measurement α, and N is the number of measurements. Minimizing (Eq. 4.1) is equivalent to maximizing

$$\mathrm{Tr}\left(\mathbf{R}^T(t)\sum_{\alpha=1}^{N}\hat{s}_\alpha(t)\hat{s}_\alpha^T(0)\right) \tag{4.2}$$

$$\mathrm{Tr}\left(\mathbf{R}^T(t)\mathbf{B}(t)\mathbf{A}^T\right) \tag{4.3}$$

for which the solution is

$$\mathbf{R}(t) = \mathbf{U}(t)\mathbf{V}^T(t) \tag{4.4}$$

where by singular value decomposition

$$\mathbf{U}(t)\mathbf{\Sigma}(t)\mathbf{V}^T(t) = \mathbf{B}(t)\mathbf{A}^T \tag{4.5}$$

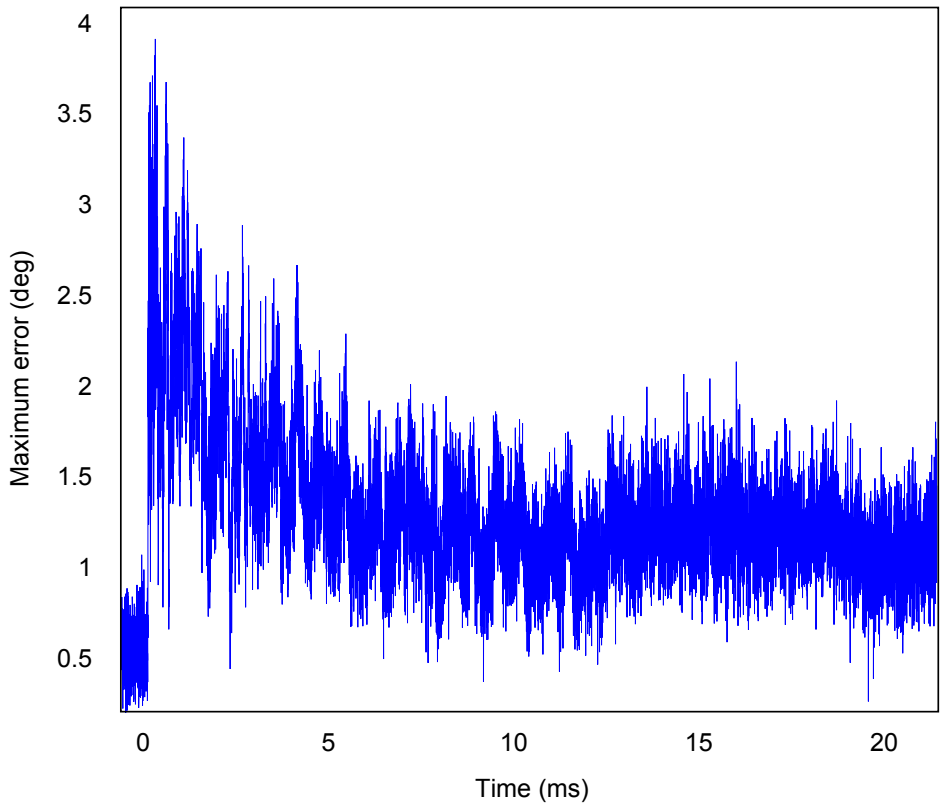

Figure 4.1: The maximum error between the SOP calculated from the rotation matrix and the measured SOP for a single measurement of the rotation vector

$\mathbf{B}(t)$ is a matrix of the SOP at time (t) for all the input polarizations, and $\mathbf{A}$ is $\mathbf{B}(t)$ at $t = 0$.

The accuracy with which the rotation matrix is determined depends on the orientation of the input SOPs. Of course a measurement for which the input SOP is coincident with a previous input SOP negligibly improves the accuracy of the estimated rotation matrix. We can determine the precision of the rotation matrix by comparing the measured Stokes parameters as a function of time to the product of the time-dependent rotation matrix and the corresponding initial Stokes parameters. The angular error for each data point is calculated using (Eq. 4.6).

$$\text{error}(t) = \arccos\left(\frac{2 - |R(t)\hat{s}(0) - \hat{s}(t)|^2}{2}\right) \tag{4.6}$$

The maximum error as a function of time for a typical measurement, shown in Fig. 4.1, does not exceed 5.0° for any measurements while the mean is less than 1.0°.

4.1.2 Rotation Axis and Angle

To extract the rotation axis and angle of rotation from the time dependent rotation matrix, we apply[7] (Eqs.4.7–4.10). However, a rotation is not uniquely represented by its rotation axis and angle. That is, if $\hat{a}$ is a rotation axis with rotation angle θ then so is $-\hat{a}$ with a different rotation angle $-\theta$. Further, an angular change of $2\pi k$ of course still represents the same rotation for any value of k. We accordingly select the axis and angle in order to ensure that the rotation vector varies smoothly with time. To do this, we select either $-\hat{a}$ or $\hat{a}$ as the rotation axis depending on which of these two minimizes the angular separation between the axis at the previous time step and the axis at the current time step. The angle for the chosen axis is then incremented if required by an appropriate multiple of 2π to avoid discontinuities. This procedure ensures that the rotation vector, $\vec{v}(t)$, and angles are smoothly varying functions of time.

$$\theta(t) = \arccos\left(0.5 \times (\mathrm{Tr}(\mathbf{R}(\mathbf{t})) - 1)\right) \tag{4.7}$$

$$\vec{r}(t)\times = \mathbf{R}(\mathbf{t}) - \mathbf{R}(\mathbf{t})^T \tag{4.8}$$

$$\hat{a}(t) = \frac{\vec{r}(t)}{|\vec{r}(t)|} \tag{4.9}$$

$$\vec{v}(t) = \theta(t) \cdot \hat{a}(t) \tag{4.10}$$

4.2 Rotation Vector Analysis

The rotation matrix for an impact is independent of the input SOP. Therefore once the rotation matrix is known as a function of time, the output SOP can be determined by multiplying the initial SOP by the rotation matrix. That is, noting that the change in SOP for a given rotation is a function of the angle between the initial SOP and the axis of rotation such that

$$\hat{S}(t) = \mathrm{R}(t)\hat{S}(0) \tag{4.11}$$

the rotation matrix can be expanded as

$$\mathrm{R}(t) = \mathrm{I}\cos(\theta) + (1 - \cos(\theta))\hat{a}\hat{a}^T - \hat{a} \times \sin(\theta) \tag{4.12}$$

which yields

$$\hat{S}(t) = \mathrm{I}\cos(\theta)\hat{S}(0) + (1 - \cos(\theta))\hat{a}(\hat{a} \cdot \hat{S}(0)) - \hat{a} \times \hat{S}(0)\sin(\theta) \tag{4.13}$$

$$\hat{S}(t) = \cos(\theta)\hat{S}(0) + (1 - \cos(\theta))\hat{a}(\cos(\phi)) - \sin(\theta)\sin(\phi)\hat{n} \tag{4.14}$$

Here $\hat{n}$ is a vector orthogonal to both $\hat{S}(0)$ and $\hat{a}$.

$$\begin{aligned}\hat{S}(t) \cdot \hat{S}(0) = &\cos(\theta)\hat{S}(0) \cdot \hat{S}(0) + (1 - \cos(\theta))(\cos(\phi))\hat{a} \cdot \hat{S}(0) \\ &- \sin(\theta)\sin(\phi)\hat{n} \cdot \hat{S}(0)\end{aligned}$$

$$\hat{S}(t) \cdot \hat{S}(0) = \cos(\theta) + (1 - \cos(\theta))(\cos^2(\phi)) \tag{4.15}$$

Accordingly, if $\cos(\theta)$ is not unity, the difference between $\hat{S}(0)$ and $\hat{S}(t)$ depends on ϕ such that the angular distance between $\hat{S}(t)$ and $\hat{S}(0)$ is the inverse cosine of (Eq. 4.15).

4.2.1 Spectrum of SOP

The frequencies of oscillation of the SOP and the rotation vector can be employed to partially quantify the polarization evolution after impact. We determine the frequency spectrum of the time evolution of the SOP and rotation vector after impact from (Eq. 4.17).

$$y_i(f) = DFT(x_i) \tag{4.16}$$

$$Y(f) = \sqrt{y_1(f)^2 + y_2(f)^2 + y_3(f)^2} \tag{4.17}$$

in which x_i, for $i = 1, 2, 3$ are the time dependent Cartesian components of the vector and $DFT(\cdot)$ is the discrete Fourier transform function.

Since the SOP depends on the input polarization, the spectrum of the SOP components also varies with input polarization. Further, the frequencies of rotations for which the rotation axis aligns with the SOP will be absent from the spectrum. Fig. 4.2 displays the frequencies of the movement of the SOPs and of the rotation vector for multiple input polarizations after a DSCM10 is impacted at position 1 (see Fig. 4.3) for a 9cm release height. The spectra associated with each of the input polarizations differ from both each other and from the spectrum of the rotation vector spectrum, as these exhibit considerable differences in the amplitudes of the different maxima and minima.

To compare the energy in the rotation of the SOP during an impact the spectral power of the oscillation frequencies of the rotation are calculated. The spectral power (Eq. 4.18), which is the integral of the spectrum of the rotation vector, can be calculated for specific frequency ranges, time ranges, or frequency and time ranges. For example, to calculate the spectral power within a certain frequency range, the endpoints of the integral are set to the limits of this range. For a time

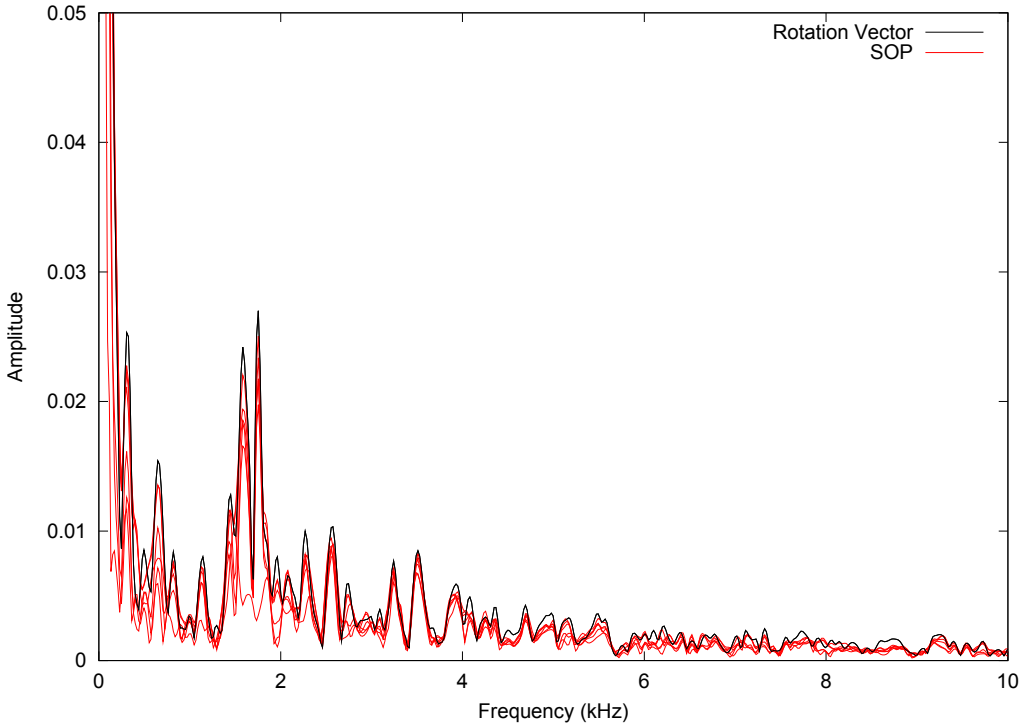

Figure 4.2: SOP component (red) and rotation vector (black) frequency spectra

range, Y (Eq. 4.17) must be calculated for the rotation vector within this interval, that is, the x_i in the previous equations are the rotation vector components during the time range.

$$Y_p = \int_{f=f_{min}}^{f_{max}} Y(f)df \tag{4.18}$$

in which Y_p is the spectral power.

4.2.2 Impact Amplitudes

The impact amplitude can be adjusted by varying the release height. The total power in the rotation vector spectrum is displayed in Fig. 4.4 as a function of release height in which each line corresponds to a different impact position. The positions of impact on the DCMs are shown in Fig. 4.3. The blue lines correspond to a DSCM10, and the red lines are the corresponding values for a DSCM20. Impacts with different release heights at the same position clearly generate similar rotation vectors (Fig. 4.5) and frequency spectra, except that the amplitude of the spectrum is smaller at lower heights (Fig. 4.6).

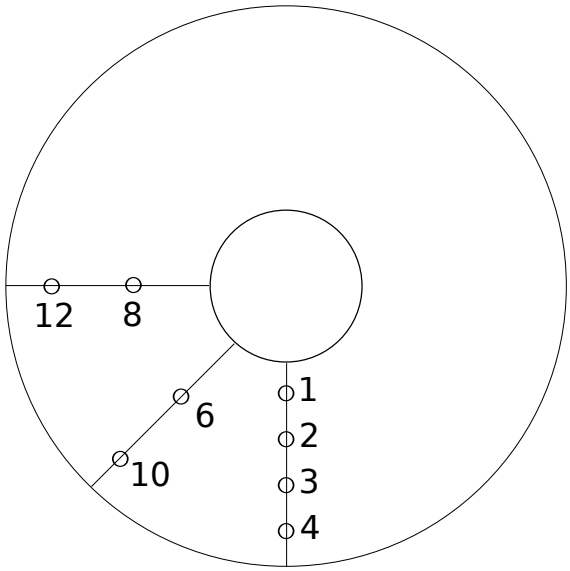

Figure 4.3: Impact positions on DCM

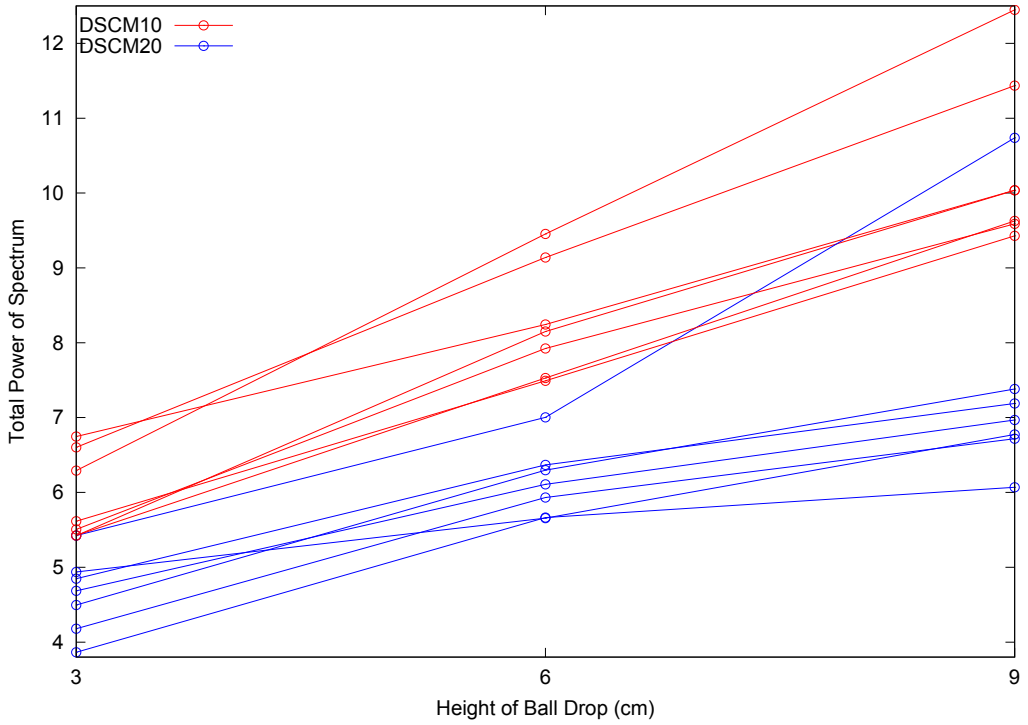

Figure 4.4: Total power in the rotation spectrum as a function of release heights for different impact locations and DCMs.

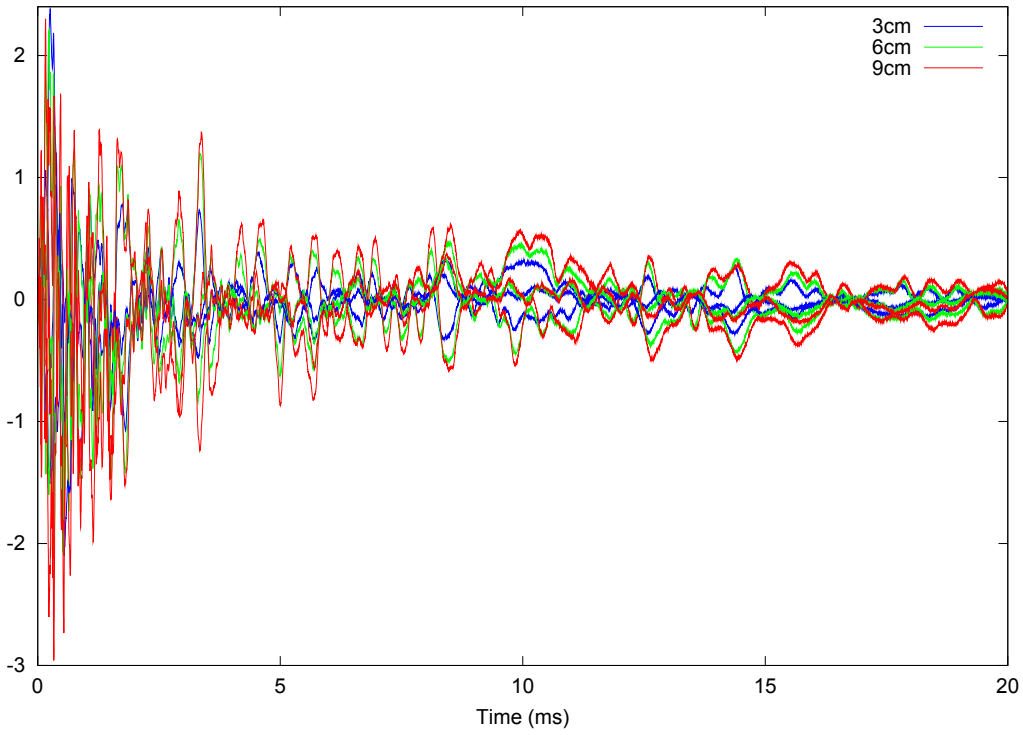

Figure 4.5: The rotation vector for different release heights for a fixed impact location on a DCSM10

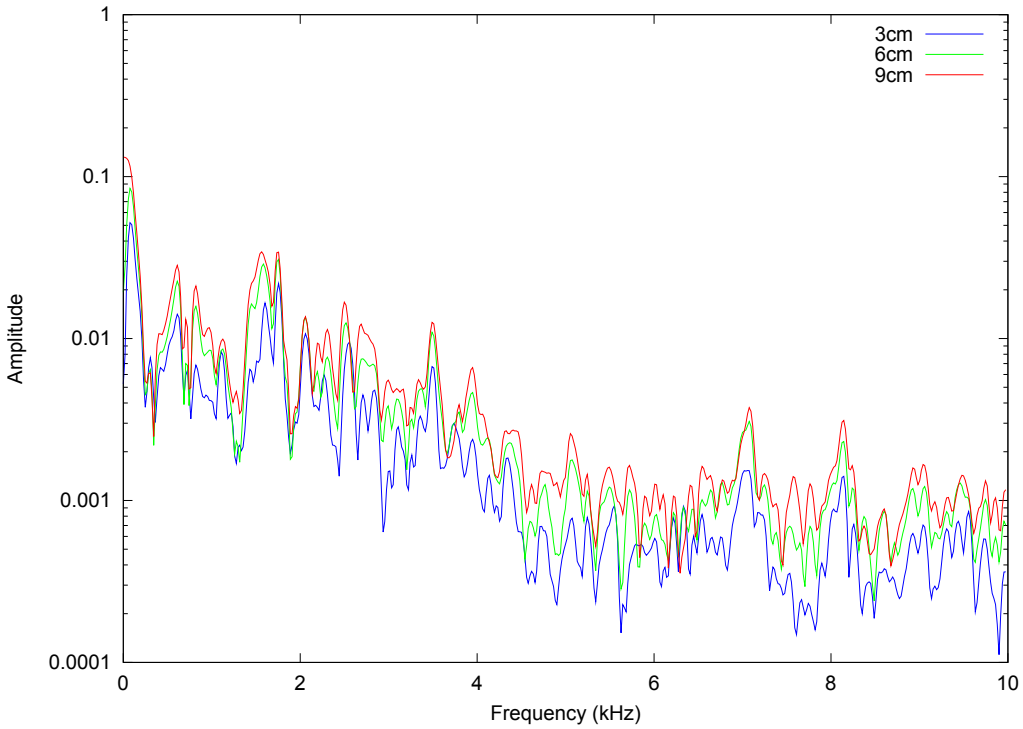

Figure 4.6: The spectrum from 0 to 10kHz of the rotation vectors for different release heights on a fixed impact location on a DCSM10

4.3 Rotation Vector Derivative

4.3.1 Numerical Simulation

The derivative of the rotation vector $\vec{V}(t)$, which can be employed to characterize the temporal response of the DCM, is more sensitive to measurement noise than the vector itself. By simulating the rotation vector as a function of time after impact, we can compare different procedures for calculating the derivative. Our model consists of a product of a series of time dependent rotation matrices, each of which has a random axis of rotation and a rotation angle that varies as a damped sinusoidal function of time. The frequencies and decay rates for the rotations are selected to emulate the measured behaviour of the rotation after impact. From our simulation, numerical values can be derived for the rotation parameters for any time t.

The simulated SOP for each input polarization at time t is calculated by applying the rotation matrix for a given time t to a random initial SOP (Eq. 4.19).

$$\hat{p}_{\mathrm{sim}}(t) = R_{\mathrm{sim}}(t)\hat{p}_{\mathrm{sim}}(t=0) \tag{4.19}$$

The variable $\hat{p}_{sim}$ denotes the simulated SOP before adding noise. Subsequently, we add a noise term with an amplitude that is chosen to coincide with that of the measured noise to the simulated SOP to simulate the observed polarization behaviour. We performed multiple measurements to evaluate the actual system noise. Each measurement was made with a random SOP. We found that the observed standard deviation of the Stokes parameters depended on the mean value of a given Stokes parameter, si according to (cf. Eq. 4.20)

$$\sigma(si) = 0.0010 + 0.0045 \cdot (1 - \overline{si}^2) \tag{4.20}$$

Here $\overline{si}$ denotes the mean of si over the measurements while $\sigma(si)$ represents the standard deviation of the Stokes parameter.

To incorporate system noise into our simulation, for each Stokes parameter a random section of a record of the sampled noise is selected. Then corresponding noise point $n(t)$ is added to the simulated Stokes parameter $\sigma(pi(t))$ at each time t according to

$$Si_{\mathrm{sim}} = \sigma(pi_{\mathrm{sim}}(t))n(t) + pi_{\mathrm{sim}}(t) \tag{4.21}$$

with

$$\sigma(pi_{\text{sim}}(t)) = 0.0010 + 0.0045 \cdot (1 - pi^2_{\text{sim}}(t)) \tag{4.22}$$

The simulated SOP including the noise at each time t is the normalized vector constructed from this sum of the Stokes parameters and the additive noise(Eqs. 4.23 and 4.24).

$$\vec{S}_{\text{sim}}(t) = [S1_{\text{sim}}(t)\ S2_{\text{sim}}(t)\ S3_{\text{sim}}(t)] \tag{4.23}$$

$$\hat{s}_{\text{sim}}(t) = \frac{\vec{S}_{\text{sim}}(t)}{|\vec{S}_{\text{sim}}(t)|} \tag{4.24}$$

4.3.2 Derivative Comparison

For reference, the standard result for the derivative of $\vec{V}(t)$ can be calculated from our simulated rotation matrix. In particular we have in Section 4.3.1 determined the rotation matrix ($R_{\text{sim}}(t)$) for any time t. In this evaluation, the two point central derivative was employed to calculate $\vec{V}(t)$ from $R_{\text{sim}}(t-\delta t)$ and $R_{\text{sim}}(t+\delta t)$ for a sufficiently small value of δt. As δt approaches zero, the two point central derivative approaches the exact derivative. We therefore employed $\delta t = \Delta t/10000$ which ensured that the squared error between the values of $\vec{V}(t)$ calculated with δt and $\delta t/2$ did not exceed 10^-2. The calculated numerical derivative of the rotation vector is shown in Fig 4.7.

The calculation of the derivative from the methods below proceeds as in the Numerical Derivative Algorithms subsection. Here, the Lanczos and Pavel methods employ either two or four degree polynomials and a variable filter length while the level of wavelet decomposition in our wavelet calculations was varied. The squared error of the derivative was then found from the sum of the square of the difference at each time t (Eq. 4.25)

$$E_{\text{sq}}(t) = \sum_{k=0}^{k=k_{max}} \left(\vec{V}(k\Delta t) - \vec{V}_m(k\Delta t)\right)^2 \tag{4.25}$$

in which $\vec{V}_m$ is the derivative of the rotation vector from one of the methods, and k_{max} is chosen so that the edge effects near the end are not summed.

For each of the methods $\vec{V}(t)$ is evaluated from the rotation vector obtained from the simulated SOP data according to the same prescription as that applied to

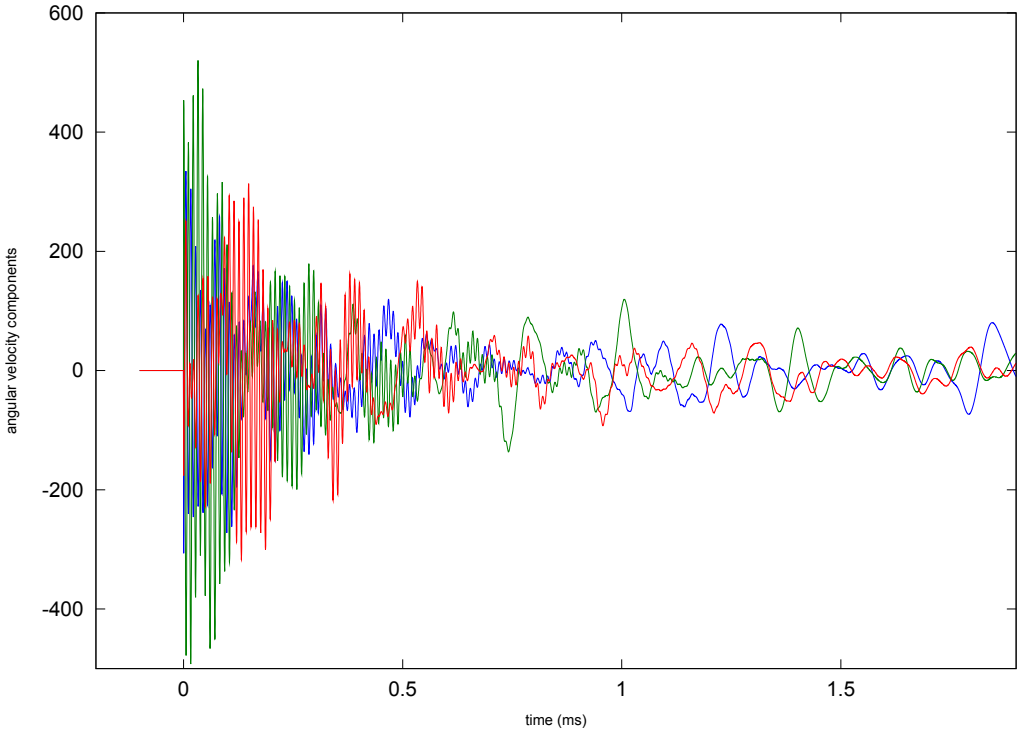

Figure 4.7: Angular velocity of the simulated rotation

the measurement data (cf. Section 4.1.2). In all cases $\vec{V}(t)$ is calculated from θ, $\hat{r}$ and the derivative of $\vec{r}$ (Eq. 4.26) according to

$$\vec{V} = (\hat{r} \cdot \vec{r}')\hat{r} + \text{sinc}\left(\frac{\theta}{\pi}\right)(\vec{r}' - (\hat{r} \cdot \vec{r}')\hat{r}) - \frac{1}{2}\text{sinc}^2\left(\frac{\theta}{2\pi}\right)\vec{r}' \times \vec{r} \tag{4.26}$$

in which $\vec{r}'$ is the derivative at time t calculated by one of the derivative methods. The Lanczos method with a four degree polynomial and a 27 point filter produced the best estimate of $\vec{V}(t)$ as can be seen from Fig. 4.8 which displays the results of all the methods and the associated errors. The calculation for the coefficients for the four degree polynomial Pavel method was only able to produce reliable coefficients up to a filter length of 21 points. The calculation required a matrix inverse that was singular to computer precision for filter lengths greater than 21 points.

For each procedure $\vec{V}(t)$ was evaluated from the rotation matrix, which again was determined from the simulated SOP data in the same manner as in the case of the measurement data(Eq. 4.4). $\vec{V}(t)$ is calculated from $R(t)$ according to (Eq. 4.27).

$$\vec{V}(t)\times = R'(t)R^{-1}(t) \tag{4.27}$$

Here $R'(t)$ is the derivative of $R(t)$, and $R^{-1}(t)$ is the matrix inverse of $R(t)$. The

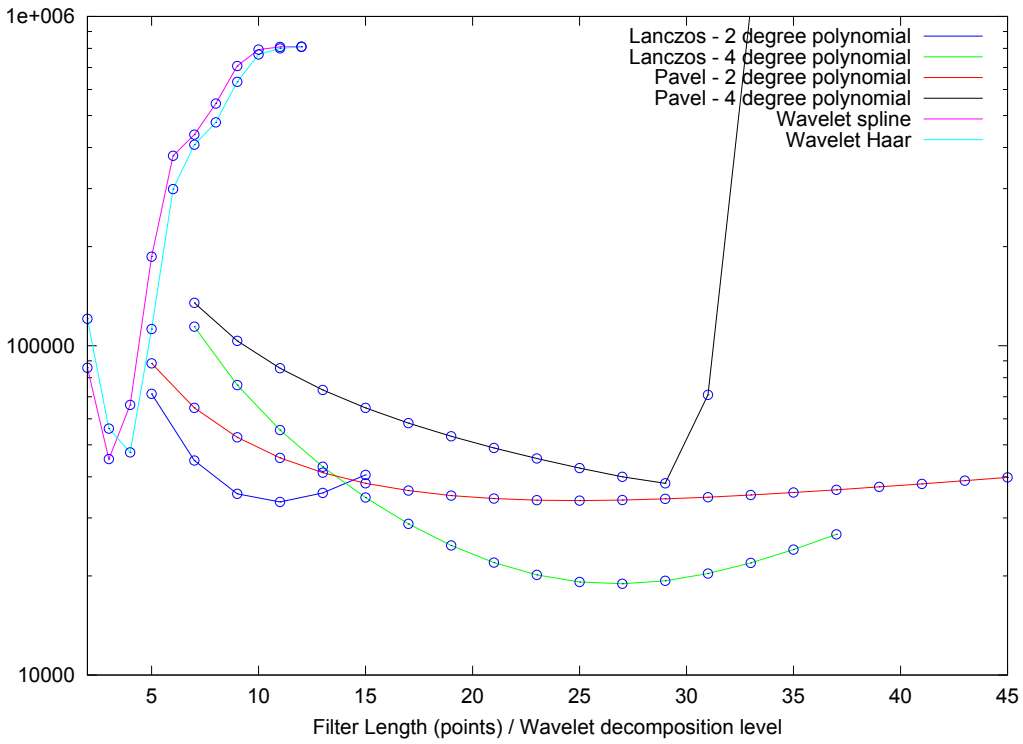

Figure 4.8: Squared error of $\vec{V}(t)$ determined from the derivatives of the rotation vector as computed from different methods with varying filter length and for wavelets, different decomposition levels.

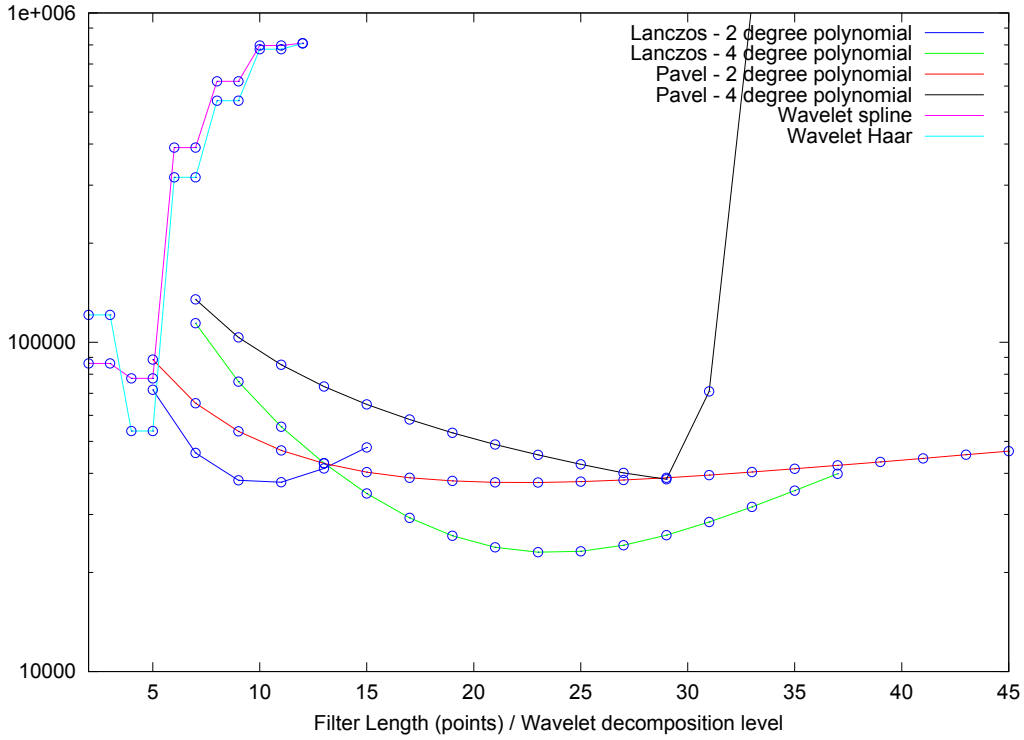

Figure 4.9: Squared error of $\vec{V}(t)$ from the derivatives of the rotation matrix for varying filter length or decomposition level of wavelets.

Lanczos method with a four degree polynomial and a 23 point filter here produced the best results, (cf. Fig. 4.9). Again the coefficients of the four degree Pavel method were inaccurate for a filter length greater than 21. As well, the calculation of the derivative from the rotation vector proved more accurate than the calculation based on the rotation matrix.

4.3.3 Numerical Derivative Algorithms

To evaluate the derivatives required in Section 4.3.2 for the rate of change of the polarization vector, we first applied the Lanczos smoothing derivative [11]. This method selects for a local set of N points within a function $f(x)$ a polynomial of size M that minimizes the cost function Z (Eq. 4.28).

$$Z = \sum_{k=-(N-1)/2}^{(N-1)/2} \left(f(k) - \sum_{j=0}^{M} a_j k^j \right)^2 \tag{4.28}$$

Accordingly we require the values of a_1 for which $\partial Z/\partial a_i = 0$.

$$0 = \sum_{k=-(N-1)/2}^{(N-1)/2} 2k^i \left(\sum_{j=0}^{M} a_j k^j - f(k) \right) \tag{4.29}$$

$$0 = \sum_{k=-(N-1)/2}^{(N-1)/2} \left(\sum_{j=0}^{M} a_j k^{(j+i)} - f(k)k^i \right) \tag{4.30}$$

for odd $j + i$

$$\sum_{k=-(N-1)/2}^{(N-1)/2} a_j k^{(j+i)} = 0 \tag{4.31}$$

therefore for odd i, even j terms cancel out and we obtain

$$0 = \sum_{k=-(N-1)/2}^{(N-1)/2} \left(\sum_{j=0}^{M} a_{2j+1} k^{(1+2j+i)} - f(k)k^i \right) \tag{4.32}$$

The constant a_1 can now be obtained from (Eq. 4.32). In calculating the derivative with the Lanczos method we employed $M = 2, 4$, and odd values of $N > 2M$.

A second group of methods are the so-called smooth noise-robust differentiators, and are referred to here as the Pavel methods[12]. The coefficients of the finite difference operator are chosen such that at low frequencies the differentiators approach the exact derivative, while at high frequencies the differentiator asymptotically approaches zero. If the numerical derivative is written as in (Eq. 4.33) we have

$$f'(x) \approx \frac{1}{h} \sum_{k=1}^{M} c_k \cdot (f(k) - f(-k)) \tag{4.33}$$

which yields the frequency response

$$H(\omega) = 2i \sum_{k=1}^{M} c_k \sin(\omega k) \tag{4.34}$$

compared to the ideal frequency response of

$$H_d(\omega) = i\omega \tag{4.35}$$

To achieve the required frequency response, the ith derivatives of H and H_d with respect to ω at $\omega = 0$ are equated for $i = 1..n$ while the jth derivative of H at $\omega = \pi$ is set to 0, for $j = 1..m$. From these equations, the coefficients c_k can be evaluated. The choice of M and n determine the value of m such that the number of equations

and unknowns is equal. In the derivative calculations for $n = 2$, $M \geq 2$, and for $n = 4$, $M \geq 3$.

We have also applied discrete wavelet transforms to calculate the derivatives. When a wavelet $\psi(t)$ is the derivative of a smoothing function ϕ, the discrete wavelet transform is the derivative smoothed by ϕ. The discrete wavelet transform is then the inner product of the signal and the wavelets. The amount of smoothing from the wavelet transform depends on the level of decomposition. A higher level smooths over a longer time while a lower level smooths over a shorter time. The 'A Trous' method was used to calculate the derivative [14]. The discrete wavelet transform of level i is calculated recursively using the following equations

$$h_i = g_{i-1} * \Psi_{h,i} \tag{4.36}$$

$$g_i = g_{i-1} * \Psi_{g,i} \tag{4.37}$$

$$h_1 = f * \Psi_h \tag{4.38}$$

$$g_1 = f * \Psi_g \tag{4.39}$$

in which $*$ represents the convolution operator,Ψ_h and Ψ_g denote the decomposition high pass and low pass filters respectively and $\Psi_{h,i}$ and $\Psi_{g,i}$ are the filters with $2^i - 1$ zeros between each value in Ψ_h and Ψ_g. The derivative for a decomposition level of n is calculated from h_i (cf. Eq. 4.40).

$$f' = -\frac{h_i}{K(2^n)^{3/2}} \tag{4.40}$$

In the expressions above K is a constant that is associated with a given wavelet. We employed Spline and Harr wavelets with multiple levels of wavelet decomposition. For Spline wavelets $K = 1$, $\Psi_h = \sqrt{2}(\frac{1}{8}, \frac{3}{8}, \frac{3}{8}, \frac{1}{8})$, and $\Psi_g = (-2\sqrt{2}, 2\sqrt{2})$. For Harr wavelets $K = \frac{1}{4}$, $\Psi_h = (\frac{\sqrt{2}}{2}, \frac{\sqrt{2}}{2})$, and $\Psi_g = (-2\sqrt{2}, 2\sqrt{2})$.

4.4 Conclusion

By considering the rotation vector, we have been able to characterize the effects of the DCM impacts on polarization in a manner that is independent of the input SOP. This however requires that the repeated impacts are largely identical. Once the rotation matrix is determined as a function of time, the SOP trace can be predicted for the impact for any initial SOP. Additionally, we have found that different forces, when applied to the same position, create similar SOP oscillations.

We also determined that the rotation vector derivatives were best evaluated with the Lanczos method using a four degree polynomial and a 27 point filter applied to the rotation vector rather than the rotation matrix.

Chapter 5

Further Applications of this Research

We have generated rapid and repeatable polarization oscillations associated with physical impacts on a dispersion compensating module and have demonstrated methods for characterizing these experimentally. These techniques can be employed in different areas of fibre optics research. For example, our measurements can be easily extended to determine the time-dependence of polarization mode dispersion and the influence and compensation of system disturbances in the presence of high-speed transients. Further investigations into these problems could therefore lead to an increased comprehension of the physical effects that can reduce quality of transmission and into procedures to counteract such disturbances.

5.1 PMD analysis

Our procedures can be directly applied to the measurement of rapid, time-dependent PMD variations. In such measurements the dispersion compensating module would be placed within the system under test. After multiple SOP measurements with differing values of the input polarization and wavelength the Müller matrix method [25] can be applied to determine the PMD. While this method normally requires two input states of polarization at two wavelengths, by performing measurements at additional wavelengths and input SOPs, increased accuracy can be achieved as long as thermal and environmental influences on the system are minimal.

5.2 Pattern Recognition

By measuring the response to impacts of differing parts of an optical communication system, disturbances in the system could potentially be identified from output polarization measurements. Resources could then be efficiently allocated to correct these effects. Different components of an optical communications system that are subject to impact and other mechanical stresses can be investigated and categorized so that a given pattern of SOP oscillations can be traced to specific equipment. As well, knowledge of these patterns could be employed to optimize the active compensation of such effects. An algorithm could recognize the initial impact signature and then predict the subsequent polarization activity resulting from the disturbance. A compensation algorithm could similarly follow from such studies.

5.3 Major Achievements

I have measured and analyzed rotational rates of SOP that to our knowledge are higher than any previously reported. I have demonstrated that impacts on DCMs yield reproducible variations of the SOP at the output of the DCM. I have also demonstrated that the impact effect can be characterized by a time dependent rotation which enables the prediction of the polarization variation as a function of time for a known impact force. Finally, I have investigated the accuracy of various methods for calculating the derivative of the rotation vector.

5.4 Conclusion

Our research has general significance for studies of high-speed optical communications systems. Application of our techniques could be employed to determine the nature of high-speed PMD variations and could possibly even be extended to the study of the influence of nonlinear effects on polarization evolution. Pattern recognition techniques could also conceivably be applied to classify and catalogue different types of oscillations according to the type of impact and the component that created the disturbance. This thesis work would then be of considerable relevance to compensation methods and algorithms for commercial optical systems.

Chapter 6

Conclusion

We have designed and realized a method for generating and measuring repeated identical mechanical impacts in optical communication system components. Here we have designed and fabricated a mechanical device for releasing a weight under precise timing conditions as well as a high-speed polarimeter that can measure the change in the state of polarization during such impacts on a dispersion compensating module. With this apparatus, we were able to measure polarization fluctuations that to our knowledge were faster than any previously measured. Perhaps more importantly, we demonstrated that the state of polarization as a function of time following the impact is highly reproducible among successive impacts. As a result, we can experimentally study properties of optical systems at high sampling rates that have not previously been accessible, such as the high-speed variation in PMD of a communications system after a physical impact. Finally, the existence of such measurement procedures could enable the application of pattern recognition methods to diagnose outage conditions generated by mechanical impacts or vibrations in a optical communications link.

References

[1] *Agilent 8509A/B Lightwave Polarization Analyzer User's Guide*, 2001. 16

[2] R.M.A. Azzam. Division-of-amplitude photopolarimeter (DOAP) for the simultaneous measurement of all four Stokes parameters of light. *Journal of Modern Optics*, 29:685–689(5), May 1982. 14

[3] M. Boroditsky, M. Brodsky, N.J. Frigo, P. Magill, and H. Rosenfeldt. Polarization dynamics in installed fiberoptic systems. pages 414–415, Oct. 2005. 11, 16

[4] John A Buck. *Fundamentals of Optical Fibers*. John Wiley and Sons, Inc, second edition, 2004. 3

[5] Morgan H.L. Chan, David Friedman, and Robert W. Donaldson. Performance enhancement using forward error corrction on power line communication channels. *IEEE Transacions on Power Delivery*, 9(2):645–653, 1994. 8

[6] Harry J.R. Dutton. *Understanding Optical Communications*. Prentice-Hall, Englewood Cliffs, NJ, 1998. 2, 7

[7] David H Eberly. *3D Game Engine Design*. Morgan Kaufmann, 2001. 40

[8] Goran Einarsson. *Principles of Lightwave Communications*. John Wiley and Sons Ltd, 1996. 7, 8, 9

[9] Dennis Goldstein. *Polarized Light*. Marcel Dekker, Inc, second edition, 2003. 2

[10] Eugene Hecht. *Optics*. Addison Wesley, 4th edition, 2002. 2

[11] Pavel Holoborodko. Low-noise Lanczos differentiators. *http://www.holoborodko.com/pavel/?page_id=242*, Jan 2009. 49

[12] Pavel Holoborodko. Smooth noise-robust differentiators. `http://www.holoborodko.com/pavel/?page_id=245`, Jan 2009. 50

[13] E. Hu, Y. Hsueh, K. Wong, M. Marhic, L. Kazovsky, K. Shimizu, and N. Kikuchi. 4-Level Direct Detection Polarization Shift Keying (DDPolSK) System with Phase Modulators. *Optical Fiber Communications Conference*, 2:647–649, 2003. 11

[14] L Jianwen, Bai Jing, and Shao Jinhua. Application of the wavelet transforms on axial strain calculation in ultrasound elastography. *Progress in Natural Science*, 16(9):942–947, 2006. 51

[15] K. Kanatani. Analysis of 3-D rotation fitting. *IEEE Trans. Pattern Anal. Mach. Intell.*, 16(5):543–549, 1994. 38

[16] Gerd Keiser. *Optical Fiber Communications*. McGraw-Hill, Inc, 1983. TK 5103.59 Kei. 9

[17] P.M. Krummrich and K. Kotten. Extremely fast (microsecond timescale) polarization changes in high speed long haul WDM transmission systems. *Optical Fiber Communications Conference*, 2(3), 2004. 11, 28

[18] Shu Lin and Jr. D.J. Costello. *Error Control Coding: Fundamentals and Applications*. Pearson Prentice Hall, second edition, 2004. QA 268 LIN. 8

[19] D. Marcuse. Pulse distortion in single-mode fibers. *Appl. Opt.*, 19(10):1653–1660, 1980. 8

[20] E.-G. Neumann. *Single Mode Fibers Fundamentals*. Springer-Verlag, 1988. 6

[21] M.J. O'Mahony. The design of a European optical network. *Journal of Lightwave Technology*, 13(5):817–828, 1995. 7

[22] M. Reimer, D. Dumas, G. Soliman, D Yevick, and M O'Sullivan. Polarization evolution in dispersion compensation modules. *Optical Fiber Communication Conference and Exposition and The National Fiber Optic Engineers Conference, Technical Digest (CD) (Optical Society of America, 2009), paper OWD4.* 15

[23] K. Thyagarajan and Ajoy Ghatak. *Fiber Optic Essentials*. John Wiley and Sons, Inc, 2007. 4, 5

[24] Gregory D. Van Wiggeren and Rajarshi Roy. High-speed fiber-optic polarization analyzer: measurements of the polarization dynamics of an erbium-doped fiber ring laser. *Optics Communications*, 164:107–120, 1999. 3

[25] Paul Williams. PMD measurement techniques and how to avoid the pitfalls. *Journal of Optical and Fiber Communications Reports*, 1:84–105, 2004. 53

[26] Peter J. Winzer and Rene-Jean Essiambre. *Optical Fiber Telecommunications V B:Systems and Networks*, chapter 2. Academic Press, 2008. 11